HAL open science

Modeling Tephra Fall and Sediment-Water Flows to Assess Their Impacts on a Vulnerable Building Stock in the City of Arequipa, Peru

J-C Thouret, E. Arapa, S. Charbonnier, A. Guerrero, Karim Kelfoun, G Cordoba, D. Rodriguez, O. Santoni

To cite this version:

J-C Thouret, E. Arapa, S. Charbonnier, A. Guerrero, Karim Kelfoun, et al.. Modeling Tephra Fall and Sediment-Water Flows to Assess Their Impacts on a Vulnerable Building Stock in the City of Arequipa, Peru. Frontiers in Earth Science, 2022, 10, 10.3389/feart.2022.865989 . hal-03902789

HAL Id: hal-03902789

https://uca.hal.science/hal-03902789

Submitted on 16 Dec 2022

HAL is a multi-disciplinary open access archive for the deposit and dissemination of scientific research documents, whether they are published or not. The documents may come from teaching and research institutions in France or abroad, or from public or private research centers.

L'archive ouverte pluridisciplinaire **HAL**, est destinée au dépôt et à la diffusion de documents scientifiques de niveau recherche, publiés ou non, émanant des établissements d'enseignement et de recherche français ou étrangers, des laboratoires publics ou privés.

Distributed under a Creative Commons Attribution 4.0 International License

frontiers | Frontiers in Earth Science

ORIGINAL RESEARCH
published: 17 May 2022
doi: 10.3389/feart.2022.865989

Modeling Tephra Fall and Sediment-Water Flows to Assess Their Impacts on a Vulnerable Building Stock in the City of Arequipa, Peru

J.-C. Thouret[1], E. Arapa[2]*, S. Charbonnier[3], A. Guerrero[4], K. Kelfoun[1], G. Cordoba[4], D. Rodriguez[4] and O. Santoni[5]*

[1]Université Clermont-Auvergne, Laboratoire Magmas et Volcans, CNRS, OPGC, IRD, Aubière, France, [2]Instituto Geofísico del Perú, Lima, Peru, [3]School of Geosciences, University of South Florida, Tampa, FL, United States, [4]Faculty of Civil Engineering, Universidad del Nariño, Pasto, Colombia, [5]Fondation d'études et de Recherches pour le développement International et Université Clermont-Auvergne, CNRS, IRD, CERDI, Clermont-Ferrand, France

OPEN ACCESS

Edited by:
Mark Bebbington, Massey University, New Zealand

Reviewed by:
Katrin Sieron, Universidad Veracruzana, Mexico
Rosario Vázquez, National Autonomous University of Mexico, Mexico

***Correspondence:**
J.-C. Thouret
j-claude.thouret@uca.fr
E. Arapa
earapa@igp.gob.pe

Specialty section:
This article was submitted to Geohazards and Georisks, a section of the journal Frontiers in Earth Science

Received: *30 January 2022*
Accepted: *29 March 2022*
Published: *17 May 2022*

Citation:
Thouret J-C, Arapa E, Charbonnier S, Guerrero A, Kelfoun K, Cordoba G, Rodriguez D and Santoni O (2022) Modeling Tephra Fall and Sediment-Water Flows to Assess Their Impacts on a Vulnerable Building Stock in the City of Arequipa, Peru. Front. Earth Sci. 10:865989. doi: 10.3389/feart.2022.865989

Arequipa, Peru's second economic center hosting c. 1,110,000 inhabitants, is the largest South American city exposed to a large variety of natural hazards. At least 200,000 live in areas likely to be affected by hazards from El Misti volcano, located 17 km to the NE. A multidisciplinary project aims to address the impacts of tephra fall and frequent mass flows on the vulnerable building stock and roofs along two ravines that cross the city, enabling decision-makers to undertake retrofitting projects and improve urban risk planning. Two recent eruptions, that is, the 1440–1470 CE Vulcanian event and c. 2070 years BP Plinian eruption, were chosen as references for probable scenarios of potential tephra fall impacts from El Misti on the building roofs. Tephra fall impacts on the city depend on the eruptive style, column height, and patterns of wind directions and velocities over south Peru and roof mechanical resistance. Estimates of potential damage levels and cost range values rely on nine structural types and four classes of vulnerable roofs. Simulation runs of hyperconcentrated flows (HCF) and debris flows (DF), using three depth-averaged flow models (Titan2F, VolcFlow, and Flo-2D) along two drainage basins on the SW flank of El Misti and across Arequipa, examined three scenarios from a database of 39 recent events and other historical lahars. Simulation results showcase the extent toward the city, inundation depths ≤4.6 m, flow velocities ≤9 m/s, and dynamic pressure up to 100 kPa from three different magnitude HCFs and DFs. In both ravines, overbank flows occurred in key urban areas due to channel sinuosity and constrictions near bridges. Potential impacts on habitat stem from ranges of flow dynamic pressure and measurements of construction material. We estimated the monetary loss of buildings according to hyperconcentrated flows and debris flows scenarios to contribute to retrofitting procedure, implementation of defense work, and relocation policy.

Keywords: tephra fall, debris flow, numerical code, building stock, vulnerability, Arequipa

1 INTRODUCTION

About three in five cities worldwide with at least 500,000 inhabitants are vulnerable to cyclones, floods, droughts, earthquakes, landslides, or volcanic eruptions or a combination of those (UN-DESA, 2018). Large cities in Latin America have no exception, as they are most prone to natural disasters. The UN Office for Disaster Risk Reduction reported about 0.50 million victims from natural disasters over the past 20 years in Latin America, and most of them are in large cities, to which environmental issues such as air and water pollution can be added. Examples over the past 20 years are floods that affected almost 4.50 million people in Peru (Alves, 2021). Based on a risk index, which considered the number of people exposed to seismic events per year (2010–2020), Peru ranked the highest with a score of 9.9 and neighboring Chile with 9.8 (Alves, 2021). Recent volcanic eruptions threatened Latin American cities such as Mexico City (Popocateptl volcano), Antigua (Fuego) in Guatemala, Pasto (Galeras) and Manizales (Nevado del Ruiz) in Colombia, Baños (Tungurahua) in Ecuador, and Ubinas (town and volcano) in Peru, to name a few (e.g., Freitas Guimarães et al., 2021).

Peru is among the foremost countries worldwide, with the largest population exposed to natural disasters (Alves, 2021). The deadliest Latin American earthquake since 1900 caused 66,000 fatalities in northern Peru on 31 May 1970, while the second strongest earthquake occurred 200 km West of Arequipa, southern Peru, on 23 June 2001 (Tavera, 2020; Alves, 2021). Although much less frequent, volcanic eruptions have created havoc at the country scale, such as the VEI 6 eruption of Huaynaputina in 1600 CE, the aftermath of which had a global climate impact (Stoffel et al., 2015). Currently, 12 active volcanoes are hazardous for the population living within a distance radius of 30 km around the active vents, while the most active Nevado Sabancaya and Ubinas, among others, are closely monitored by IGP and INGEMMET. Floods, debris flows, and landslides affected almost 4.50 million inhabitants in Peru over the past 20 years (Alves, 2021), and as many as 21,900 floods and landslides have been recorded over the past 10 years according to Civil Protection authorities.

1.1 Scope of the Study and Research Objectives

Arequipa, Peru's second-largest city (1,081,000 inhabitants as per the 2017 national census; INEI, 2018), is one of the fastest-growing regions in the country, at the contact between the Andean highlands and the coast. Arequipa is situated at c. 2,300 masl in a pull-apart basin between the west flank of the Western Cordillera of the Central Andes and the Coastal batholith to the south. This basin was filled by volcanic deposits, mostly Neogene and Pleistocene ignimbrites, covered in part by volcanoclastic deposits that make up the foothills of the Nevado Chachani, El Misti, and Pichu volcanoes. Chachani (6,080 masl) and Pichu (5,600 masl) are extinct volcanic clusters, but El Misti active composite stratocone currently exhibits seismic and fumarolic activity (Aguilar Contreras et al., 2022). Arequipa is the largest South American city exposed to a large variety of natural hazards from El Misti volcano, earthquakes, flash floods, and mass flows. Between 50,000 and 100,000 inhabitants living <1 km from active river or ravine channels are likely to be affected by flash floods and/or lahars, and many more if El Misti volcano, located 17 km NE of the city of Arequipa, produced tephra fall and PDCs. Socio-economic hardships are added to environmental hazards because poor urban development and planning have led to informal settlements and marginal contributions to improving living conditions (INEI, 2018).

The multidisciplinary project "Impacts in the City of Arequipa" aims to address hazards, exposure, and vulnerability of buildings and infrastructure that face frequent flash floods, hyperconcentrated flows (HCFs hereafter), and debris flows (DFs hereafter) along five ravines or quebradas that cross the city. The five ravines are tributaries to Río Chili (inset map, **Figure 1**), whose discharge is artificially controlled for electric supply and water intake. Impacts of potential tephra fallout have also been addressed here so that probabilities of roof collapse in case of eruption may enable stakeholders to undertake retrofitting projects and improve risk management in urban planning.

The research objectives are threefold: 1) to assess the extent of impacts of potential tephra fall on building roofs based on earlier classification of the building stock; 2) to characterize and simulate mass flows, that is, HCFs and DFs in two ravines often affected by floods in the recent past: Quebrada (Qda.) San Lazaro and Qda. Huarangal-Mariano Melgar (Huarangal-MM thereafter), draining the SSW and South slopes of El Misti, respectively (**Figure 1**); and 3) to assess impacts of these flows on the building stock in order to contribute to potential loss assessment.

1.2 Terminology

Flash floods are local floods triggered within 6 h and often within 3 h, generally resulting from heavy rainfall over a catchment (National Weather Service, 2022). Flash floods frequently occur in arid or semi-arid environments where rainfall is concentrated over a short period of time, and the infiltration capacity of the soil is limited so that runoff is triggered shortly after the rainfall onset on relatively steep slopes. Flash floods can occur in cities where construction and pavement made the ground impervious. The environment of the city of Arequipa is propitious to flash floods and mass flows as the result of the semi-arid climate (c. 150 mm a year), the concentration of rainfall as thunderstorms often delivering more rainfall than the average monthly amount. A series of factors favor FFs, HCFs, and DFs across Arequipa (See **Table 1**): (i) short-lasting (3–4 h) and intense rainstorms (26–42 mm/h, from five meteorological stations across the basin of Arequipa over the past 60 years; Fuse and Benites, 2003) typical of a semiarid climate (≤150 mm/year at 2,300 masl); (ii) rapid runoff (30–60 min) in relatively small mountainous catchments (18–40 km^2); (iii) the impervious network of roads and waterproofing of the built-up area that increase runoff; and (iv) the steep, bare slopes of El Misti's foothills carved by ravine channels, which are filled by loose volcanic debris mixed with household and industrial waste

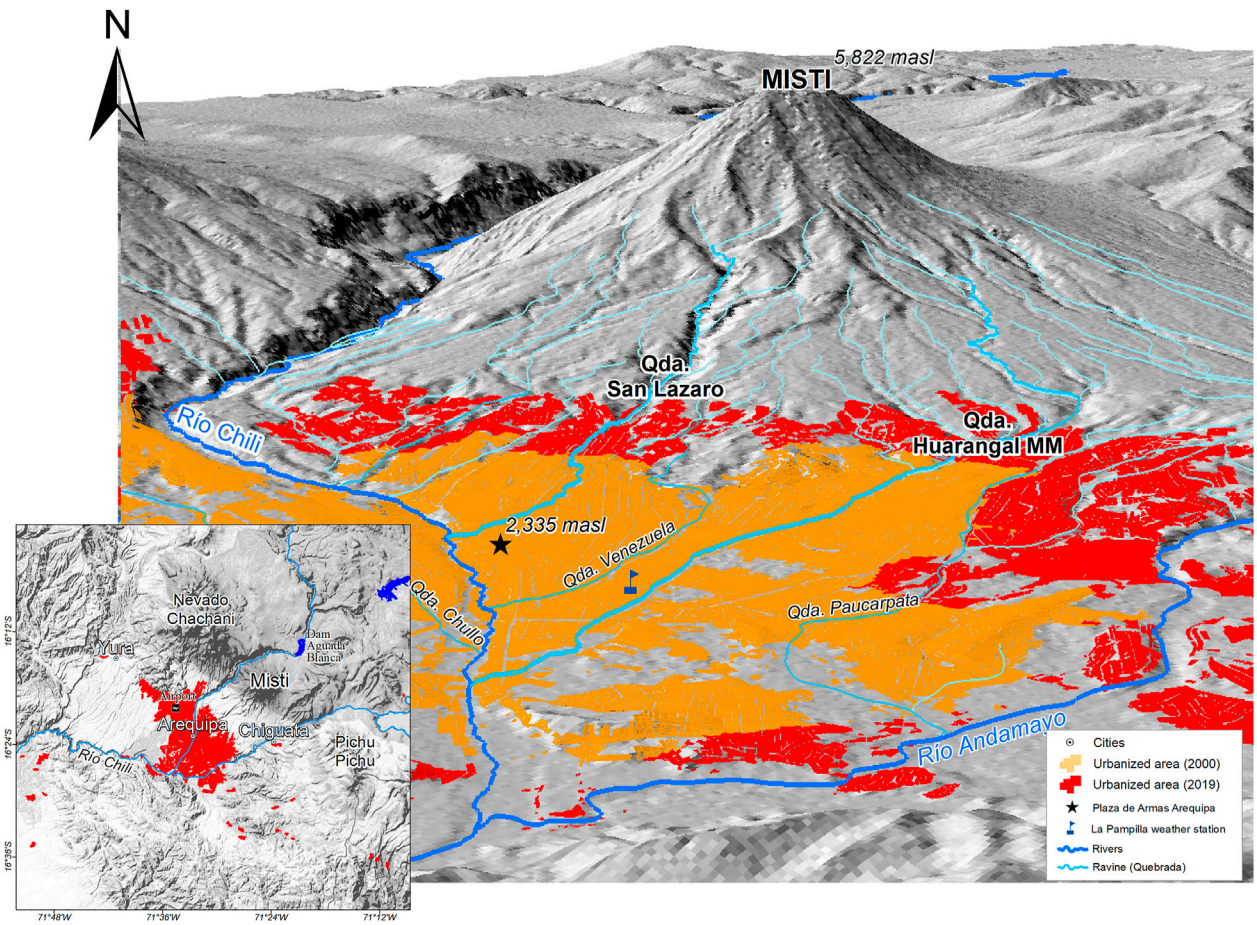

FIGURE 1 | Peripheral growth of the city of Arequipa over the past 20 years. Construction has spread out from the initial oasis and Historic center on the east Río Chili high terrace (1540–1940) onto the volcaniclastic fans SW of El Misti after 1960 and encroached the slopes of the volcano as well as the volcaniclastic apron of Nevado Chachani after 1980. Drainage network including tributaries (locally termed quebradas or torrenteras) to the main artery, Río Chili. Quebrada San Lazaro and Quebrada Huarangal–Mariano Melgar (Huarangal-MM) are the targets of this study. The meteorological station La Pampilla is indicated. Inset map shows the setting of the city of Arequipa, basin, and neighboring volcanoes (active El Misti, dormant Chachani, and extinct Pichu).

(Thouret et al., 2013, 2014; Ettinger et al., 2015; Thouret et al., 2018; Arapa et al., 2019).

Lahars (volcanic debris flows, LHs) and rain-triggered debris flows (DFs) are potentially destructive water-saturated mass flows acting in mountainous regions and areas where steep slopes cut down in loose sediment. These flows can be divided into two categories using sediment concentration, grain-size distribution, and bulk density (Vallance, 2000; Hungr and Jakob, 2005; Manville et al., 2013; Vallance and Iverson, 2015; Thouret et al., 2020):

1. Debris flows (DFs) are mixtures of debris and water with high sediment concentrations that move downslope due to gravity as surging sediment slurries (Vallance, 2000). DFs comprise a solid phase of at least 60 vol% (>80 wt%), thoroughly mixed with water. The solid component includes mostly gravel and boulders with sand, silt, and clay proportions remaining low. A threshold of 3 wt% of silt and clay helps distinguish non-cohesive from cohesive DFs (Scott, 1988; Scott et al., 2005). The density of a DF ranges between 1,800 and 2,400 kg/m^3, twice as much as the muddy water that flows in stream channels during floods (Pierson, 1980).

2. Hyperconcentrated flows (HCFs) are two-phase flows intermediate in sediment concentration between "normal" streamflows and DFs, with densities between 1,300 and 1,800 kg/m^3. HCFs transport between 20 and 60 vol% (40 and 80 wt%) of sediment (Beverage and Culbertson, 1964; Pierson, 2005).

2 METHODS AND DATA ACQUISITION

A combination of methods has involved field surveys and digital data collection, mapping and GNSS surveys for improving the high-spatial-resolution (2–4 m) digital terrain model (DTM), and numerical codes for simulation, as well as assessment of impacts on and potential loss of habitat and bridges.

Surveys at the local scale of neighborhoods (city blocks) along two ravines (Qda. San Lazaro across the north and central parts of

TABLE 1 | Statistical data that result from the database of flow and rainfall events in Arequipa between 1915 and 2020 (see Table). Rn = number of recorded flood/flow events. Sn = number of significant (i.e., causing fatalities and damage) flood/flow events. See **Supplementary Table S1** displays the flow and rainfall events database.

Flow event no.	Average 1915–2020	Flow type %	Monthly occurrence %	Rainfall event Total, intensity, and duration					Rio Chili discharge*** (n = 23)		Fatalities (Rn = 39 Sn = 21)		Affected people (Rn = 21;Sn = 21)		Reported damage (Rn = 39; Sn = 21)				
				Average total rainfall ** n = 14	Average Intensity.	Maximum Intensity	Critical int. threshold	Rainfall duration Average n = 19	Maximum	Average	Total	Average	Total	Average	House		Bridge		Cost US$ million 8 Feb
					Intensity, mm/h (n = 28)										Total	Aver	Total	Aver	
Recorded Rn = 39	2.70	FF 55 HCF 33 DF 12	Jan 33 Feb 54 March 13	76.9 mm	25.30	41.5	24-26	4h19	340 m^3/s	130 m^3/s	N = 39 34	N = 39 0.88	32,656	838	7,610	196	23	0.59	1989 = 0.7 19-20 March
Significant* Sn = 21	4.78	FF 57 HCF 27 DF 16	Jan 22 Feb 64 March 14	79.7 mm	30.10	41.5	28.5-30	4h17	-	-	N = 21 34	N = 21 1.62	32,656	1,556	7,610	363	23	1.10	2001 = 1.8 8 February 2013 = 130

the city and Qda. Huarangal-MM across the NE part of the city, **Figure 1**) allowed us to collect geometrical and technical data (**Supplementary Table S2**) on the building stock using a GIS, data collector, and mapper device (Trimble TC 1000) at the city block or building scale to assess the building stock performance. GIS mapping used high-resolution Pléïades satellite images and Google Earth Pro. A high-spatial-resolution (2–4 m) digital elevation model (DEM) (Oehler et al., 2014) was based on Pléaïdes satellite imagery (2013) using stereophotogrammetry. A digital surface model (DSM) was also produced recently (see Charbonnier et al., 2020 for details) by taking out the obstacles (e.g., bridges) along the ravines in order to avoid excess deposits and subsequent overbank upstream of the bridges. Channel constriction and sinuosity must be accounted for, and its effect must be assessed. GNSS data collection was achieved during two field campaigns throughout the area of the city to tie the DEM to ground control points and two geodetic monuments (Instituto Characato, USGS in Characato, and Instituto Geofísico del Perú in Cayma).

2.1 Assessment of the Potential Impact of Tephra Fall

1. We used probabilistic maps of tephra fall extent and load from El Misti on the city and surrounding areas produced by Sandri et al. (2014). Taking into account past events according to the recorded eruptive styles, the authors ran many simulations using TEPHRA2 (Connor and Connor, 2011) for each type of eruption and volumes of tephra fall between 10^6 and 10^9 m^3. Using a Bayesian event tree and elicitation method, the authors measured a 0.05% tephra-fall probability of occurrence over 1 year for Arequipa in case of Vulcanian, SubPlinian, or Plinian eruption, particularly during the wet season (December–March). Their study provided four maps showing the areal distribution of probabilities of tephra fall with two mass loading thresholds, 100 and 250 kg/m^2, of tephra loads exceedance on roofs for both rainy and dry seasons and two, 10 km and 20 km columna heights (**Figures 6**, **7** in Sandri et al., 2014).

2. We assessed the vulnerability of roofs with respect to tephra load, including two steps: i) field surveys helped us recognize nine types of constructions and roofs based on several criteria collected by means of field surveys across 300 city blocks and ii) classification of about 2,000 buildings was achieved by means of field surveys at the building scale, completed by remote sensing using high-spatial-resolution Pléïades satellite images and drone images (50 and 25 cm pixel, respectively) and Google Street View (**Figures 3A–D**).

2.2 Evaluation of Impacts, Loss, and Cost of Water-Rich Flows on Habitat

1. We elaborated a database of flow events over the period 1915 to 2020 to highlight hydrological input parameters that will be used in numerical simulations (See **Table 1**; **Supplementary Table S1**).

TABLE 2 | Morphometric parameters of the catchments of Qda. San Lazaro and Qda. Huarangal-MM.

Ravine quebrada	Length km	Orientation	Slope %	Gradient	Maximum elevation	Minimum elevation	Watershed area	Watershed perimeter
					Masl	Masl	km^2	km
San Lazaro	14.1	NE-SW	9.2	0.10	3,674	2,371	18.80	30.0
H-MM	20.2	ENE-WSW	5.5	0.05	3,375.5	2,256	26.90	41.10

2. We chose two catchments, namely, the Qda. San Lazaro and the Qda. Huarangal-MM, which initiate >3,300 masl on the SW flank of El Misti volcano, for two reasons: they have been often affected by flash floods and mass flows, and their channels run across a wide range of buildings representing different periods of construction from suburbs to the historic center of Arequipa in the medial and distal reaches, respectively. All ravines, usually dry, become active during the rainy season (December to March) when they convey flash floods and mass flows to Río Chili. **Table 2** displays a few morphometric characteristics of both catchments.

Qda. San Lazaro forms high (3,680 masl) on the SW flank of El Misti volcano and follows a NE-SW direction over a length of 14.1 km with an average slope of c. 8° from its source to its confluence with Río Chili near the Grau Bridge (2,372 masl) (**Figure 2A**). The catchment area is 18.80 km^2. The ravine has incised past lahar and pyroclastic-flow deposits a few tens of meters thick, forming two steep (9%) and widespread (5.50 km × 1.80 km) fans, which have been entirely built over the past 50 years. Qda. San Lazaro has been diverted to the SW, 1 km upstream of the confluence with Río Chili, by the older, eastern fan, which merges down valley with the high terrace supporting the historic center (Thouret et al., 2014). The longitudinal profile of San Lazaro shows three reaches and a gradient of 0.10 (**Figure 2A**). Nine bridges were built over Qda. San Lazaro, the most vulnerable being José Olaya, Parque Selva Alegre, and Ingreso Universidad Católica San Pablo (**Figure 2A**; Thouret et al., 2014).

The source of Qda. Huarangal-MM is located at 3,270 masl on the South flank of El Misti volcano, and the ravine follows an ENE–WSW direction, over a length of 18.9 km with an average slope of 5.3° from its source to the confluence with Río Chili near the suburb Tingo (2,259 masl; **Figure 2B**). Several tributaries join Qda. Huarangal-MM, but the c. 50-m-wide channel narrows down valley near the Geronimo–Paucarpata suburb. As a result, the Huarangal-MM catchment is more extensive than that of San Lazaro (**Figure 2C**; **Table 1**), while its longitudinal profile with a gradient of 0.05 is half as steep as its counterpart (**Figure 2B**). Five amongst ten bridges that cross the ravine are more vulnerable: 8 de Octubre, Tupac Amaru, Jorge Chavez, Santa Rosa, and Gran Unidad Escolar (**Figure 2B**; Thouret et al., 2014).

3. We utilized three numerical codes, Titan2F, VolcFlow, and FLO-2D, to simulate mass flows. Our purpose is to test the abilities of these numerical codes to simulate DF and HCF events and detect their limitations compared with real cases derived from field data or previous simulations described in the literature.

4. We assessed mass-flow impacts on habitat and drew fragility curves involving hydrodynamic and hydrostatic pressure (*via* flow depth) from DF and HCF, resulting from simulations and earlier studies (Mead et al., 2017; see Thouret et al., 2020 for a review of lahar characteristics and impacts). This assessment was completed by *in situ* measurements on home and bridge construction material, both on walls and common construction material, using devices such as sclerometers for hardness and compressive strength, an ultrasonic analyzer for crash resistance, Young's modulus, and surface velocity (Chehade, 2021).

5. Using results from fragility curves for two categories of building wall thickness, we computed loss fractions for the most vulnerable classes A0, A, and B according to the position of buildings adjacent to two ravine channels and the delineated area of simulated dynamic pressure near both ravine channels. From the building loss fractions, we estimated the cost of reconstruction or retrofitting for each vulnerable class of A0, A, and B according to the percentage of building loss fraction in case of DF and HCF.

3 CITY GROWTH AND HAZARDS

The urban area of Arequipa remained relatively compact, mainly on the eastern margin of the Río Chili valley, now the Historic center and UNESCO heritage, from its foundation in 1540 CE until the 1960s (population 86,000) (Gutiérrez, 1992; Thouret et al., 2013; Thouret et al., 2014; Thouret, 2018; Thouret et al., 2018). The population grew rapidly from 81,000 in 1940 to 309,100 inhabitants in 1970, at a rate of c. 6% per year. From 1970 onward, Arequipa has concentrated the largest economic investment in the region, which accelerated people's out-migration from rural areas, also influenced by a succession of droughts on the Altiplano and social unrest in the 1990s. These processes all caused massive out-migration from highlands which contributed to a poorly planned urbanization, poorly designed suburbs, and peripheral low-income settlements that continue to date to the north, northeast, and west of the historic city (Gutiérrez, 1992; Thouret, 2018; Thouret et al., 2018; INDECI, 2019). In 60 years (1970–2020), the built-up area has grown ninefold, from 13 to approximately 115 km^2 (**Figure 1**). As a result, the overall population of Arequipa has increased by more than 330%. Constructions now occupy two-thirds of the basin on both sides of the Río Chili valley and have long encroached upon the lower flanks of El Misti and its western neighbor, Nevado Chachani, as far as 15 km from the historic center, in the form of poorly designed suburbs and "illegal" settlements at the

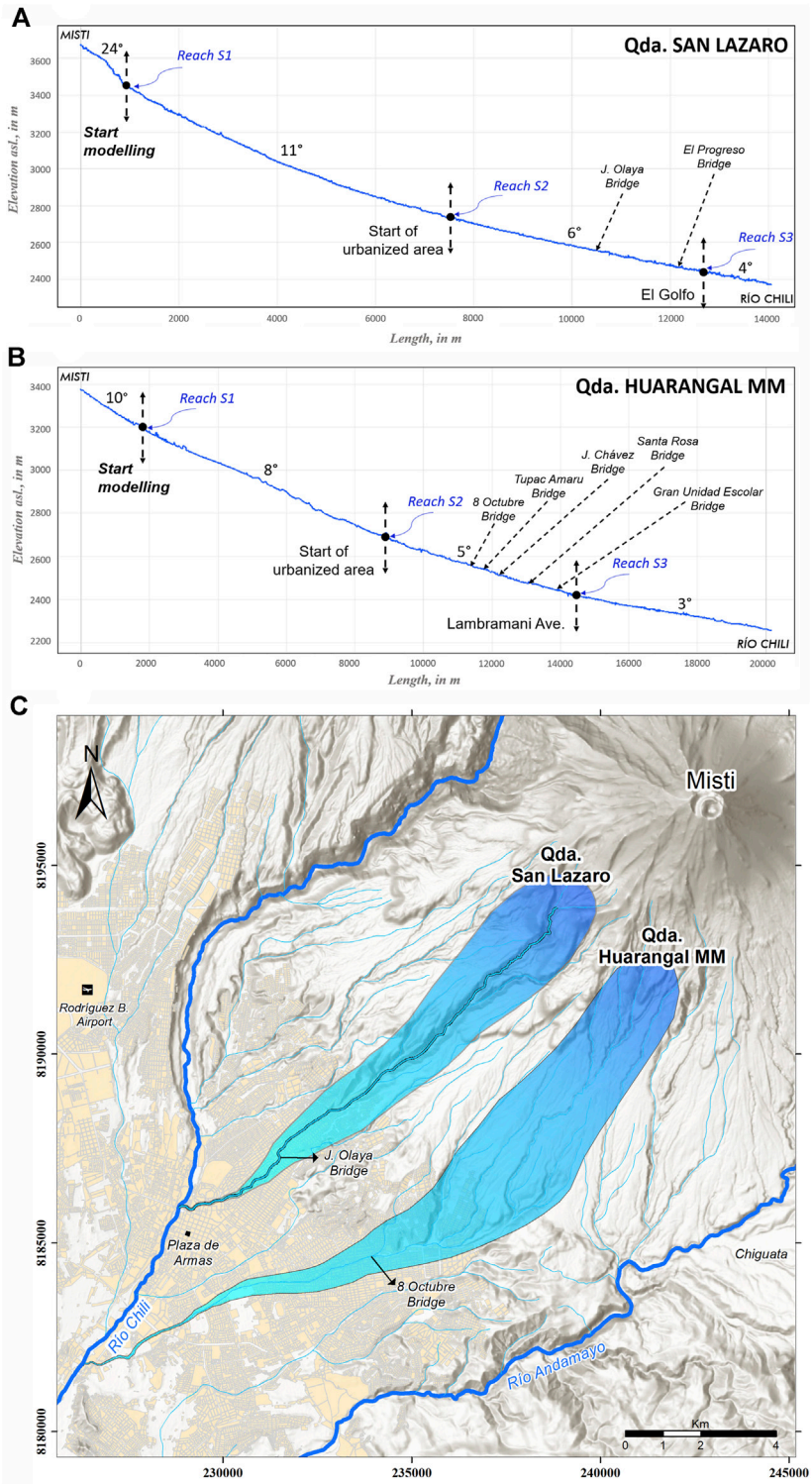

FIGURE 2 | Catchment and longitudinal profiles of the Quebradas (ravines): **(A)** Qda. San Lazaro (SL) and **(B)** Qda. Huarangal-MM. **(C)** Outline and extent of the drainage basins of the two ravines under study. Bridge locations and names are indicated along both ravine profiles. See **Table 1** for morphometric parameters of both catchments.

TABLE 3 | Classification of building and roof types (about 1,500 buidlings in 3,000 city blocks) and estimated vulnerability based on seven criteria in districts adjacent to Qda. San Lazaro and Qda Huarangal-MM (Method after the Plinius Study Centre, *in:* Thouret et al., 2013, 2014 for details). We added estimated cost ranges for each class based on construction or rental cost (per m^2) as of 2018–2019.

Structural typology	Building material, structure and roof	Vulnerability class	Cost range, $US
1	Make-shift housing	A0	≤200
1A	Masonry of lapilli concrete with roof made of metal sheet (1 storey)	A0	250–500
1B	Masonry of ignimbrite without mortar with roof made of metal sheet (1 storey)	A0	250–500
2A	Masonry of terra cotta with roof made of metal sheet (1 storey)	A0	400–700
2B	Masonry of ignimbrite with mortar with roof made of metal sheet (1 storey)	A0	500–800
3A	Masonry of terra cotta with reinforced concrete roof, with structural deficiencies (1–2 storeys)	A	5,000–20,000
3B	Masonry of terra cotta with reinforced concrete roof (1–2 storeys)	A	10,000–30,000
4	Masonry of terra cotta confined in reinforced concrete (RC) frame with RC roof (1–3 storeys)	B	30,000–80,000
5	Masonry of ignimbrite (1,500) with mortar with masonry vaults: historical building (1–2 storeys)	A	100,000–300,000
6A	Masonry of ignimbrite (1,500) modified with RC elements and raisings of type 3 (2–3 storeys)	B	200,000–400,000
6B	Masonry of ignimbrite (1,500) modified with RC elements and raisings of type 8 (2–5 storeys)	B	200,000–400,000
6C	Masonry of ignimbrite (1,900) modified with RC elements (2–3 storeys)	B	200,000–400,000
7	RC buildings without seismic design with RC flat roofs (2–4 storeys)	C	200,000–400,000
8A	New RC buildings with RC pitched roofs (1–2 storeys)	D	200,000–450,000
8B	New RC buildings with RC flat roofs (3–8 storeys)	D	300,000–700,000
8C	Buildings with RC walls and RC flat roofs in the historic center	D	400,000–700,000

periphery. By 1990, urban expansion had engulfed areas that were otherwise bare in 1945, such as the extensive volcanoclastic fans formed by Qda. San Lazaro and Qda. Huarangal-MM. **Figure 1** further displays the city growth area between 2000 and 2019.

Hazard assessments based on the geologic mapping of deposits and previous simulations of volcanic and non-volcanic mass flows, using LaharZ and Titan2D, indicate that the city is highly exposed to natural hazards (Thouret et al., 1995; Thouret et al., 1999; Thouret et al., 2001; Delaite et al., 2005; Mariño et al., 2007; Vargas Franco et al., 2010; Martelli 2011; Cobeñas et al., 2012; Cobeñas et al., 2014; Thouret, 2018). The most threatening hazards for Arequipa, set in impact and frequency order, are the destructive (Mw ≥ 8) earthquakes with a 10% probability exceedance in 50 years (Aguilar et al., 2017); 2) the potentially destructive (VEI 2–4) eruptions of the active El Misti with an estimated recurrence of 500–2,000 years (Thouret et al., 2001); and 3) the low-to-moderate magnitude ($0.1–1 \times 10^6$ m^3) and high-frequency (2.7 years on average) flash floods and mass flows (**Table 1**; **Supplementary Table S1**).

3.1 Tephra-Fall Hazard

Potential volcanic hazards from the active El Misti are acute, as the recorded eruptive activity exhibited a variety of styles and deposits (Thouret et al., 2001; Harpel et al., 2011; Charbonnier et al., 2020). Among the volcanic hazards (**Supplementary Figure S1**), we focus on tephra fallout, while modeling of PDCs has been the target of recent work (Charbonnier et al., 2020). Tephra fall is considered the most common hazard from volcanic activity. It has rarely caused human life loss, but the high mobility of small particles is responsible for health problems and has economic impacts in cities around active volcanoes. Globally, the impacts of tephra fall include building roof collapse, damage to aircraft, disruption of lifelines, and health and environmental effects. Tephra fall from El Misti occurred in the mid-15th century in Arequipa and fine ash from Nevado Sabancaya in 2016. However, explosive activity over the past 50,000 years has shown a succession of Vulcanian to Plinian eruptions and a frequency of about 500 years for VEI 2 events and 2,000–5,000 years for VEI 3-4 events (Thouret et al., 2001; Sandri et al., 2014).

Holocene and historical Misti's activity has encompassed a range of eruptions with VEI 2-4 magnitudes. Two recent eruptions (i.e., the 1440–1470 CE Vulcanian event and the ca. 2070-year BP Plinian eruption) are working references for probable scenarios (e.g., Sandri et al., 2014). Tephra-fall deposits at least 10 cm thick were emplaced by the mid-15th-century event (Chávez, 1992; Thouret et al., 2001), while 2070-year BP pumice-fall deposits exceeding 50 cm in thickness have been observed across the city area (Cobeñas et al., 2012; Cobeñas et al., 2014; Harpel et al., 2011; Harpel et al., 2013). Dispersal of tephra fallout toward the city depends principally on the eruptive style, column height, and patterns of wind directions and velocities over southern Peru.

3.2 Floods and Mass-Flow Hazards

Mass flows including DFs and HCFs threaten the city area, to which flash floods (FF) are added in the semi-arid environment of southern Peru. We selected 39 FFs and mass-flow events over the period 1915–2020 from reports, newspapers, and previous studies (e.g., Fernandez-Davila and Benites Montufar, 2003) that we completed with INDECI (National Institute of Civil Defense) reports (2019) on disasters (**Table 1**; **Supplementary Table S1**). As a result, FFs and lahars (HCFs or DFs) occur every 2.7 years on

TABLE 4 | Building roof types and vulnerability classes based on eight criteria. **Barrio de invasion:* "illegal" settlement, settlement without basic needs given to new migrants for a small amount of money or with the purpose to obtain electoral support or political influence. ***Size or area:* small (<100 m^2), medium size (100–300 m^3), large size (300–1,000 m^2), very large size (>1,000 m^2).

BUILDING ROOF TYPE 9 categories	Small house or modern pavilion 1	Regular quality house, suburb 2	Recent, high-income house 3	Regular- to poor-income house, suburb & *"barrio de invasion"** 4	School or administration building 5	High-rise, modern building 6	Composite, low- income business, shelter, shabby house 7	Historic monuments, old, maintained buildings 8	Sport or leisure facility areas, open market, gas station 9
Roof slope	Flat or single pitched	Flat	Pitched	Flat	Flat	Flat	Flat or low angle	Rounded Vaulted mansonry	n.a. (not applicable)
Construction material & cover	Cement slab with concrete beams or tiles cover	Metal sheet (zinc, corruga-ted iron)	Concrete slab with RC beam; Tiles	Light material (tent, plastic or wood) on cement slab	Brick or cement slab, with RC beams	RC slab	Heterogeneous (cement, wood, light) above weak ceiling	Ignimbrite or concrete with beams	Open or tent (linen or plastic)
Building use	Habitat (house)	Industrial, business, supermarket habitat	Modern or decorated house	House or shelter; Un-finished (partly open sky)	Several storey-house or building	Residential and/or offices	Shed, garage or business; unfinished (open sky)	Church Convent, Government	Sport
Roof size (area) **	< 100 m^2	100 to 200 m^2	200–300 m^2	<100 m^2 and 100–200 m^2	300–500 m^2	500–1,000 m^2	≤100 m^2	300–600 m^2	500–>1,000 m^2
Number of storeys	1	1	2 or 3	1 or 2	≥2	>3	1 or 2	High	n.a.
Maintenance	Good	Regular to poor	Very good	Regular to poor	Regular	Good	Poor conditions	Sturdy	Regular
Period of construction	10 to 30 years ago	20th century	10 to 20 years	20th century or recent 'invasion'	20 to 50 years	10–20 years	20th century	16–19th century	10 to 40 years
Roof,resistance Collapse threshold (kPa)	Good (4–6)	Poor (1.5–3)	High (5–10)	Poor or structurally deficient (1–3)	Good (5–10)	High (7–12)	Poor or structurally deficient (≤2)	High (7–10)	Poor or n.a. (1–2)
Roof vulnera-bility class	C	**B**	D	**A**	C	D	**A**	D	**A**

average and can be lethal and destructive every 5 years on average (**Table 1**; Nagata, 1999; Thouret et al., 2013; Thouret et al., 2014; Xue, 2016). The disrupting flows affected about 33,000 inhabitants and damaged more than 7,600 buildings over the past 105 years (**Supplementary Table S1**; Regional de Arequipa, 2014; INDECI, 2019). One of the destructive and lethal events occurred on 8 February 2013 when heavy rainfall (124.5 mm during 3 h) triggered an HCF and extensive flood along the Qda. Venezuela, affecting 280 buildings and 23 bridges in the city (Ettinger et al., 2015).

4 BUILDING STOCK AND ROOF CLASSIFICATION

To assess potential damage, we mapped and ranked the structural types and vulnerable classes of the building stock across 300 city blocks, including about 1,500 buildings. Two additional campaigns in 2018 and 2019 enabled us to complete the structural classification at the house scale along both quebradas (**Supplementary Figure S2**) (Thouret et al., 2013; Thouret et al., 2014). Field surveys collected data such as usage, quality of the construction material, surface area, structural support, openings, and roof types for the building performance (**Table 3**; **Supplementary Table S2**), completed through remote sensing using two high-spatial-resolution Pléaïdes satellite images as of 2013 (Thouret et al., 2014). Prieto et al. (2018) quantified the relationship between hazard intensity and building performance. The structural characteristics bearing on the resistance of buildings to mass-flow hazards include weight-to-breadth ratio, structural yield and/or ultimate lateral capacity, and associated model parameters (α_1 and λ). In order to compute these ultimate parameters for building resistance, a handful of variables need to be collected in the field and from imagery: building height, length and weight/breadth, inter-story height, thickness and density of walls, slab weight over the floor area ratio, the vertical axial stress on the base of walls, and masonry shear resistance. In addition to these structural elements most pertinent for the structural types to be

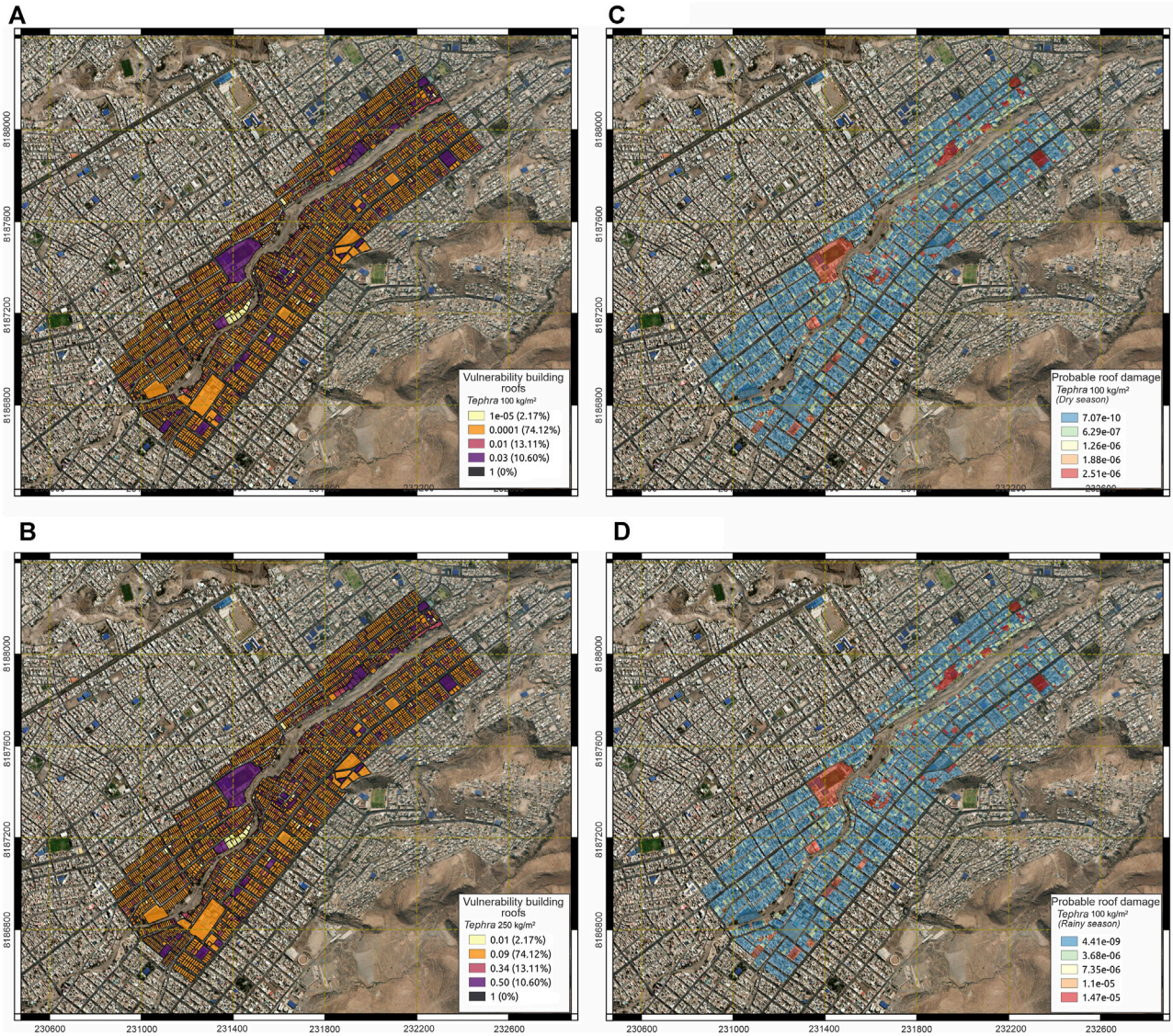

FIGURE 3 | Areal distribution and vulnerability index of roof classes along the medial reach of Qda. San Lazaro according to **(A)** Tephra mass loading of 100 kg/m^2 and **(B)** Tephra mass loading of 250 kg/m^2. Evaluation of roof damage probabilities in the medial reach of Qda. San Lazaro for **(C)** Tephra mass loading of 100 kg/m^2 and **(D)** Tephra mass loading of 250 kg/m^2.

identified, we add the edifice shape, presence or lack of master design, and resistance of the construction material.

Eight structural types of buildings were classified based on structural support, prevailing construction material (brick, masonry, concrete, ignimbrite, or adobe), openings, and roof type, among others (Thouret et al., 2014). A series of 15 architectural and structural characteristics helped determine the least to the most vulnerable building classes (**Supplementary Table S2**). The structural types have been summarized and ranked according to four vulnerability classes A0, A, B, and C (**Table 3**; **Supplementary Figures S2, 3**). Distinct vulnerability classes were supported by an inventory of heavy, significant, and slight damage levels observed on buildings in the wake of the 2013 disastrous HCF along Quebrada Venezuela (Ettinger et al., 2015).

Typical building materials in Arequipa differ from the rest of Peru and usage helped us rank them. 1) Bricks and masonry that have been present in Peru since 1916 represent >62% of the construction materials due to the prevalence of clay soils and new technologies. Industrial bricks exhibit homogenous dimensions and higher resistance to compression than artisanal bricks. 2) The "sillar," an unwelded white ignimbrite, represents 23% of construction materials (INEI, 2018); the use of sillar increased after the 1582 earthquake that left the city of Arequipa in ruins (Silgado, 1978). The sillar now used for the construction of monuments and hotel or residence facades stems from

TABLE 5 | Structural description and vulnerable classes of roofs with estimated range of construction cost. Vulnerability index and damage value. Inset graphics represent tephra load vs thickness for two tephra-fall deposits taken as probable eruptive scenarios of El Misti, i.e., the mid-15th Century vulcanian event (maximum 10 cm thickness over the city area) and the c. 2070 yr BP Plinian eruption (maximum 50 cm thickness over the city area). Damage value after Blong et al (2017): 0 No damage; 1 Light damage (gutters), cleanup required; 2 Moderate damage, bending or excessive damage to as much as half roof sheeting and/or purlins, Interior requires cleaning, repainting, and/or overhaul of electrical systems; 3 Heavy damage to roof structure and some damage to walls; at least one wall damaged. Collapse of part of ceiling.

Roof Type	Vulnerability class (after Blong)	Description after Blong et al. (2017), modified and adapted to the Arequipa case (see Table for details)	Surface area (10^3 m^2)	Area proportion %	Estimated range of construction cost, US$
1	C	Flat or single pitched, cement on timber rafters/trusses, in good condition. Tiles on timber trusses, in average or good condition	606.814	66.75	1000–2000
2	B	Long span, flat roofs with metal sheet or fibre reinforced concrete sheets, in average condition	119.220	13.10	≤200
3	D	Pitched roofs on timber rafters/trusses, in average or good condition, or concrete slab with RC beams	10.423	1.15	2000–4000
4	A	Flart roof, weak timber boards on timber rafters/trusses; Light material roof on timber rafters/trusses, in old or poor conditions	13.556	1.50	100–200
5	C	Flat roof, brick or cement slab on timber rafters/trusses, in good condition; fibre reinforced in average or good condition	66.972	7.35	2500–5000
6	D	Flat rooof, RC slab on strong timber rafters/trusses in good condition	8.511	0.95	3000–7000
7	A	Flat or low-angle roof, heterogeneous or light material on weak timber boards, in poor condition, rafters/trusses; Metal sheet roof on timber rafters/trusses, in old or poor conditions	17.814	1.95	100–200
8	D	Vaulted mansonry roofs, concrete or ignimbrite masonry with strong timber rafters/trusses, in good condition	0.769	0.10	2000–5000
9	A	Open area without roof or light material (tent, pastic), no timber or weak timber boards, in average or poor condition	65.023	7.15	≤200

Building Class	Vulnerability to tephra mass load 100 kg/m^2	Vulnerability Index	Vulnerability to tephra mass load 250 kg/m^3	Vulnerability Index	Central damage value
A	0.03	V1	0.50	V3	0.4
B	0.01	V0	0.34	V2	0.1
C	0.00010	V0	0.09	V1	0.03
D	0.00001	V0	0.01	V0	0

quarries along the Añashuayco ravine west of Arequipa Airport, where the Arequipa Airport Ignimbrite is mined (Paquereau-Lebti et al., 2006; Paquereau-Lebti et al., 2008). More fragile construction materials such as wood and corrugated iron represent 10%, according to the information collected in the 2017 census. Adobe is much less common at ≤5%, compared to ≥25% for the country (INEI, 2018).

4.1 Structural Types of Roofs and Potential Impacts of Tephra Fall

Structural classification of nine roof types (**Table 4**), based on Blong et al. (2017) classification and field surveys, encompasses mostly habitat buildings and administrative, educational and religious edifices, historic monuments, and sport facilities. Types 1, 2, 3, 4, and 6 are houses and residential buildings, while types 5, 7, 8, and 9 correspond to commerce and other edifices (**Supplementary Table S4**; **Supplementary Figure S3**). We defined five types of residential habitats ranging from houses with poor quality of construction material (e.g., type 4) to residential, 2 + story buildings for which design, structure, and material offer better resistance to load and impacts. Poor quality and vulnerable houses either have roofs made up of light material (plastic, wood, zinc, or a combination of those) or are often unfinished constructions without a roof. Type 2 average quality houses and commerce or industrial buildings have metal roofs and better-quality materials. Types 1 and 3 are high-quality and resistant buildings, while type 3 edifices show a better design and roof resistance due to pitch and reinforced concrete. Type 6 includes high-rise edifices with reinforced concrete, and potential impacts from tephra fallout have been estimated in terms of probabilities. The impacts would be more important during the rainy season when wind patterns would disperse more tephra toward the city area (**Figures 6**, **7**inSandri et al., 2014). We assessed the extent of roof damage by comparing the tephra load (in particular 250 kg/m^2) with the least resistant buildings and roofs that belong to vulnerability classes A0 and A. The latter classes prevail along the upper and middle reaches of both quebradas (**Supplementary Figure S2**).

We refer to Sandri et al. (2014) for the probability maps of tephra fall with 10 or 20 km high eruption column heights, wind patterns, and velocities during two dry and wet seasons in southern Peru and for two hazard metrics (tephra loads of 100 and 250 kg/m^2). We evaluated the structural performance and

TABLE 6 | Estimate of discharges and return periods of mass flows in Quebradas compared with discharges and return periods of Río Chili floods obtained using a Gumbel distribution.

Recurrence interval (years)	2	5	10	50	100
Discharge m^3/s Quebradas	19	45	85	124	160
Discharge m^3/s Río Chili	62	110	142	238	340

susceptibility of roof collapse across built areas along both banks of Qda. San Lazaro and Qda. Huarangal-MM. Each building roof was classified based on seven criteria, including quality of the construction material, usage, and surface area. We obtained nine types of roofs mapped in the Q-GIS software.

4.2 Vulnerability Index of Roofs and Probable Damage

The nine roof types have been converted into four vulnerability classes (Blong et al., 2017) according to the mechanical resistance of the material and based on two hazard metrics 100 and 250 kg/m^2. These tephra loads, in turn, yield pressures of 1–2 kPa and forces of 1,000 and 2,500 N/m^2 (inset graphics, **Table 5**). A substantial proportion (38% in area) of regular-quality roofs may not withstand 250 kg/m^2 or 2.5 kN/m^2, and almost all low-quality roofs (11%) may suffer structural damage or collapse if the tephra load reaches 100 kg/m^2 or 1 kN/m^2. Particular attention was paid to light and heterogeneous material covering low-quality houses, ranked as "hybrid" roofs, which can be affected by minor tephra loads ≤100 kg/m^2. Flat roofs or upper ceilings without proper cover may be more vulnerable than pitched roofs, a category that represents 3%-4% (in area) only of the surveyed buildings located in high-income neighborhoods only. Both values of hazard metrics may increase in case of rainfall concomitant with tephra fall because the probability of ashfall toward the city increases during the rainy season (Sandri et al., 2014). Both values of forces (1–2.5 kN/m^2) are 2.5–6 times lower than forces exerted by tephra thickness between 20 and 50 cm in case of Plinian tephra fall (inset graphics, **Table 5**), to be compared to the 50-cm-thick 2070 BP pumice-fall deposit observed in the north and NW areas of the city.

The vulnerable roof classes rely on structural description and mechanical resistance (**Table 4**), which has led to impacts according to damage level in case of tephra fall exceeding the tephra loads and forces defined above (**Figures 3C,D**). From maps of vulnerable roofs and vulnerability index (**Figures 3A,B**; **Table 5**), we estimate three damage levels in case of the higher hazard metrics (load of 250 kg/m^2 defined above): 1) heavy/severe (i.e., roof collapse and burnt timber, failure of trusses and supporting structure, severe to moderate damage to rest of the edifice) for roof types 4, 7, and 9 (c. 11% in area); 2) significant damage to the roof structure and some damage to walls, at least one wall damaged/misaligned, collapse of part of ceiling for roof type 2 (c. 13%); and 3) slight (bending, damage to roofs overhangs and ceilings without roof, required cleaning, repainting or material overhaul) for roof types 1 and 5 (c. 14%). If the tephra load exceeded 250 kg/m^2 and reached about 6 kN/m^2, which would be the case with a 50-cm-thick tephra fall comparable to the c. 2070 BP Plinian pumice-fall (i.e., between 5 and 6 kPa), the aforementioned roof types (categories A, B, and C; **Table 4**) would all experience collapse, while moderate-to-severe damage would affect the rest of edifices. If we consider the probability of roof collapse triggered by a combination of tephra load (250 kg/m^2) and rainfall, the proportion will increase to the majority of roof categories beyond classes A, B, and C, except for the RC (reinforced concrete) and pitched types of roofs, category D.

We estimated the cost of roof construction in case of damage due to tephra mass loading (inset graphics, **Table 5**), considering at least 425 building roofs along the medial reach of Qda. San Lazaro together with the proportion and estimated cost range of each roof type (**Table 5**). Severe damage of 75% of low-quality roof types 4, 7, and 9 would amount to a range of 18,000–20,000 US$. Significant damage of 50% of regular-quality roof type 2 would reach 6,000–8,000 US$, while slight damage of 25% of average-quality roof types 1 and 5 would translate into a cost range of 75,000–80,000 US$.

5 RECORD OF SEDIMENT-WATER FLOWS

The analysis of a 105-year database (1915–2020) in Arequipa helped describe the key characteristics of rainfall and flow events (**Table 1**; **Supplementary Table S1**).

5.1 Characteristics and Occurrence of Flash Flood and Mass-Flow Events

Flash floods were the most frequent events (55%), while HCF represented 33% and DF only 12% of the total events. Because solid concentration was not measured *in situ*, DFs with at least 40% vol. solid concentration may actually be more frequent. All flow events occur during the rainy, austral summer, with the majority (54%) in February, 33% in January, and 13% in March. Over 105 years, one event occurred every 2.70 years on average. A significant flow event (i.e., with >1 fatality and damaged buildings and/or bridges) occurred every 5 years on average.

Rainfall Events Triggering Flows/Floods

Considering the recorded rainfall intensity for 28 recorded events that triggered flows lasting 1.5–3 h, the average rainfall intensity is 25.30 mm/h. Maximum intensity rainfall reached c. 41 mm/h, according to Fuse and Benites (2003). We estimate the critical rainfall intensity to be in the range of 25–26.5 mm/h, increasing to 28–30 mm/h for more destructive and lethal flow events. In fact, the critical threshold depends on the total rainfall during 24 h or preceding days and the duration of the triggering rainfall (see below). As many as 21 events spanned 2 to 5 days of intermittent rainfall. The average rainfall intensity was 31.1 mm/h, and the maximum was 41.5 mm/h during the 8 February 2013 flow. Most flows were triggered just before or during the maximum rainfall intensity.

The duration of the rainfall events ranges between 2 and 8 h. The average was 4 h and 19 min for 19 rainfall events that

TABLE 7 | Comparison of input parameters used in mass-flow numerical simulations (from the literature) compared to our simulations using Titan2F, VolcFlow and FLO-2D codes.

Input Parameters	Unit	Model used	Publications[a]		Our simulations	
			HCF	DF	HCF	DF
Volume	$\times 10^5$ m^3	VF, T2F, Fl2D	1.0–6.0	1.0–6.0	1.5–5.0	1.5–5.0
Solid concentration	%vol.	T2F, Fl2D	20–50	50–80	30–40	60–70
Yield strength	Pa	VF, Fl2D	<50	<400	1–20	50–100
Bulk density	kg/m^3	VF	1,300–1,800	1,800–2,300	1,300–1,600	1,900–2,200
Viscosity	Pa.s	VF	0.1–10	<50	0.01–1	10–50
Internal friction	degree	T2F	20–35	20–35	20–33	20–33
Basal friction	degree	T2F	10–20	10–20	10–18	10–18
Manning's coefficient		Fl2D	0.01–0.1	0.01–0.1	0.03–0.08	0.03–0.08
Froude number		Fl2D	<1 (subcritical flows)	<1 (subcritical flows)	0.9	0.9
Laminar flow resistance		Fl2D	24–50,000	24–50,000	400	400
Peak discharge	m^3/s	Fl2D	10–500	10–500	20–400	20–400
Volumetric discharge	m^3/s	VF, T2F, Fl2D	20–1000	20–1000	25–300	25–300
Duration	s	VF, T2F, Fl2D	14,400	14,400	7,200–10,800	7,200–10,800

VF = Volcflow, T2F = Titan2F, Fl2D =FLO-2D.

[a]*Woohliser, 1975; Pierson and Costa, 1987; Phillips and Davies, 1991; Rickenmann, 1991; Major and Pierson, 1992; O'Brien et al., 1993; Iverson et al., 2010; Martelli, 2011; Manville, 2013; Charbonnier et al., 2017; Thouret et al., 2020 (references therein).*

triggered flows. The total precipitation over 24 h on average was 76.9 mm for 14 recorded rainfall events with a minimum of 30.5 and a maximum of 190.2 mm. On 8 February 2013, the meteorological station La Pampilla (monitored by SENAMHI, 2013) registered 124 mm of rain during 3 h, which was a c. 100-year return period rainfall event.

5.2 Mass-Flow Characteristics

Ettinger et al. (2015) reported some characteristics of the 8 February 2013 HCF. Total volume of the flow ranged between 50,000 and 100,000 m^3. Peak flow discharge increased from 124 m^3/s in the upstream reach to 425 m^3/s in the middle reach, and the average discharge was seven times that of average discharge (19,50 m^3/s) of streamflows (maximum 43 m^3/s in San Lazaro and 69 m^3/s in Huarangal-MM; Fuse and Benites, 2003) occurring in the rainy season. Velocity ranged between 5.9 and 10.9 m/s and flow depth between 3 and 6 m. The return period of discharges in Quebradas using the Gumbel distribution was compared to the case study of Río Chili (Martelli, 2011) and estimated on the basis of discharges reported from the 2013 event (**Table 6**).

Reported Fatalities and Damage Caused by Significant Flow Events

Twenty-one flood/flow events induced victims and significant damage that was measured *in situ* or estimated afterward. For example, extensive damage was reported for two events in 1989 and 2013; the 8 February 2013 flow killed five persons and affected 22,970 people. About 4,540 homes were affected and 150 were destroyed, while 10 bridges were badly damaged (INDECI, 2019).

Fatalities totaled 34 persons over 105 years, yielding 0.88 fatalities on average per flow event, but we counted as many as 32,656 affected (displaced, homeless, or injured) people. On average, 838 people were affected per flow event, a figure doubling in case of destructive or lethal events. The total number of affected buildings is estimated to be 7,610, that is, 196 per flow event or 363 per destructive flow event. As many as 23 bridges were reported to have been damaged by flow events over the period 1915–2020.

6 COMPLEX MASS-FLOW RHEOLOGY AND MODELING

The sediment-water flows, including HCFs and DFs, exhibit a complex flow behavior determined by physical and rheological properties (Pierson and Costa, 1987; Phillips and Davies, 1991; Rickenmann, 1991; Major and Pierson, 1992; Iverson, 1997; Rickenmann, 1999; Lavigne and Thouret, 2003; Iverson, 2014; Iverson et al., 2011; Manville et al., 2013). The complexity and variability of HCF- or DF-properties during their propagation make them difficult to characterize and thus define a physics-based model. According to Takahashi (2014), some models consider a single-phase continuum fluid or two-phase continuous fluid (mixture theory), such as the Newtonian fluid, Coulomb-viscous fluid, Bingham fluid, Herschel–Bulkley fluid, and dilatant fluid (George and Iverson, 2014). Furthermore, the dynamic behavior of lahars/DFs has led to a variety of modeling approaches, ranging from simple empirical models to physics-based models (Manville et al., 2013). DFs exhibit a behavior that may be compatible with the Bingham viscoplastic fluid, the viscosity of which is independent of shear rate (Major and Pierson, 1992; Manville et al., 2013), which can reach up to 1.5 order of magnitude greater than the viscosity of HCFs. Viscosity strongly depends on sediment concentration and the amount of silt and clay (Bardou et al., 2007). DFs possess a yield strength that can vary from tens to hundreds of Pa, which must be lower than the shear stresses, and alike viscosity is also very sensitive to the sediment concentration (Phillips and Davies,

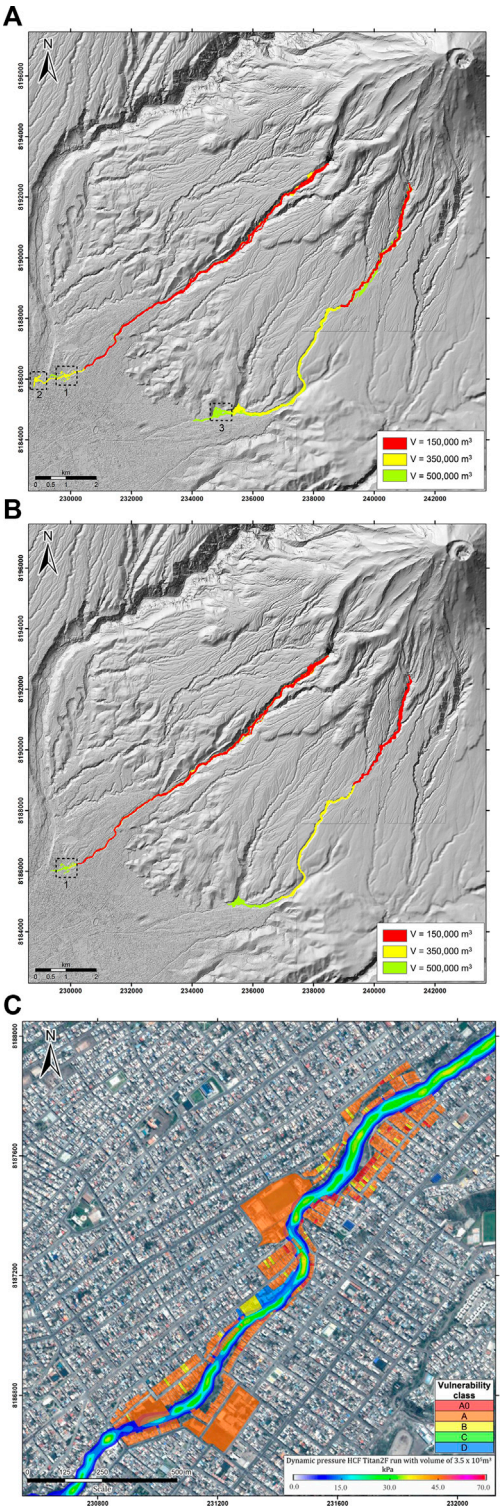

FIGURE 4 | (A) Titan2F-simulated HCFs with a range of three volumes (1.5, 3.5, and 5 × 10^5 m^3) in Qda. San Lazaro and Qda. Huarangal-MM. Rectangle #1 shows the overbank near the Progreso bridge down valley San Lazaro. Rectangle #2 shows damming by a moderate volume DF and subsequent runup at the confluence of Río Chili. Rectangle #3 indicates the overbank area in the Geronimo–Paucarpata suburb in Huarangal-MM, similar

(*Continued*)

FIGURE 4 | to the actual overbank area inundated in 2011. **(B)** Titan2F-simulated DFs with a range of three volumes (2.5, 3.5, and 5 × 10^5 m^3) in Qda. San Lazaro and Qda. Huarangal-MM. **(C)** Distribution of HCF dynamic pressure (using Titan2F) in the middle reach of Qda. San Lazaro with a volume of 3.5 × 10^5 m^3.

1991; Major and Pierson, 1992; Iverson, 2005). When the complex behavior of DFs or lahars needs to be described, the presence and interactions of the two (solid and fluid) phases cannot be neglected (Iverson et al., 2010; Iverson, 2014).

HCFs typically possess a small but still measurable static yield strength of a few tens Pa, which can increase as it is strongly influenced by the amount of fine material (Rickenmann, 1991; Pierson, 2005). The viscosity is between 10^2 and 10^4 times greater than the viscosity of water, which is strain-rate dependent (Julian and Lan, 1991; Phillips and Davies, 1991). Pierson (2005) described HCF as an intermediate flow type between streamflow and DF, with a highly suspended, fine sediment concentration, while coarse sediments are transported as bedload. Therefore, they exhibit a turbulent two-phase behavior (Rickenmann, 1991; Manville et al., 2013). Considering the properties of HCF, such as density and viscosity, several authors have defined its behavior as a pseudoplastic fluid flow.

6.1 Modeling Debris Flows and Hyperconcentrated Flows

In recent decades, various computational models have been developed that have allowed simulating the physics of mass flows from the resolution of equations by numerical methods (Iverson, 2014). Computational models or numerical codes have become one of the most important tools for HCF/DF hazard assessment. Thouret et al. (2020), their **Table 4** elaborated on a list of models used for simulating lahars or HCFs/DFs, such as LAHARZ-py (Schilling, 2014), Titan2D (Pitman and Le, 2005; Williams et al., 2008) and Titan2F (Córdoba et al., 2015; Córdoba et al., 2018), FLO-2D (O'Brien et al., 1993), RAMMS (Cesca and D'Agostino, 2008), and VolcFlow (Kelfoun and Druitt, 2005). We tested three models, Titan2F, VolcFlow, and FLO-2D, all shallow-water depth-averaged models for modeling HCFs and DFs in the Qdas. San Lazaro and Huarangal. Assuming that HCF or DF thickness is much smaller than its length, it is possible to integrate the 3D mass and momentum balance equations over depth to obtain the depth-averaged continuum flow equations (Savage and Hutter, 1989). All simulations were performed over the 2013 DSM of the El Misti-Arequipa area (Oehler et al., 2014; Charbonnier et al., 2020) after smoothing and resampling the grid to 4 m spatial resolution and removal of all bridges crossing both Quebradas to avoid artificial blocking of the channeled flows. Charbonnier et al. (2020) used another couple of Pléaïdes images to enlarge the DSM to the SW flank and a TanDEM-X (12 m) to include the NE of the city, Huarangal-MM catchment, and El Misti's summit. This has led to a DSM where bridges and other obstacles have been removed to simulate "free" flows, avoiding artificial damming and thickening of flows in case of

TABLE 8 | Input parameters used to simulate HCFs and DFs with Titan2F numerical code and output parameters for three different scenarios.

Scenarios	Input parameters			Output parameters			
	Volume *V*	Time	Initial solid concentration	Volume *V*	Time	Mean velocity *v*	Volume *V*
	$\times 10^5$ m^3	Min	Vol%	$\times 10^5$ m^3	Min	m/s	$\times 10^5$ m^3
T1	1.5	240	T1	1.5	240	T1	1.5
T2	3.5	240	T2	3.5	240	T2	3.5
T3	5.0	240	T3	5.0	240	T3	5.0

artificial obstacles. We also ran simulations using the original DTM in which bridges and obstacles were present: the artificial obstacles (i.e., bridges digitally represented as vertical walls) dammed channeled flow deposits and induced artificial overbank flows with high velocities (5–7.5 m/s). Based on the outputs of the computational models, we defined mass-flow inundation zones, flow depths, and dynamic pressure and compared the results from the three codes despite their different purposes and input parameters.

The computational models require several input parameters (either from measurements in river channels and flumes, empirical models, or literature) and initial and boundary conditions, which are different for the three models (**Table 7**). In order to apply reliable rheological models to the modeled flows, we defined the density, viscosity, and yield strength parameters for each type of flow. Among required input parameters, flow rate and sedimentation concentration are critical for simulating sediment-water flows. Despite the lack of recorded flow discharges (except for streamflows and a few recent events, e.g., the 8 February 2013 HCF), we estimated discharges for both Quebradas based on the available discharge data of Río Chili and the Gumbel law distribution (**Section 5.1**; **Table 6**). The paucity of sedimentation concentration values makes it difficult to apply rheological properties and determine flow behavior, representing critical input information for modeling. Pallares et al. (2015) found high sand and gravel contents and a minimum amount of fine particles in historical lahar deposits across the city of Arequipa, although it is known that the grain-size distribution of lahar deposits does not reflect the wide flow spectrum that emplaced them (Dumaisnil et al., 2010). In case of heavy rainstorms (≥41 mm/h) over the small catchments under study, erosion and incorporation of coarse-grained volcaniclastic deposits to lahars may produce a limited increase in fine-grained particles (<8% silt and clay; Pallares et al., 2015). A small proportion of clay and silt in flows would influence the behavior of less cohesive HCFs and DFs (Bardou et al., 2007). Thus, we derived additional physical and rheological parameters of the flows to be simulated from previous studies of lahar characteristics at Sarno, Italy (Zanchetta et al., 2004); Mt. Ruapehu, New Zealand (Manville et al., 1998); Semeru, Indonesia (Dumaisnil et al., 2010; Doyle et al., 2010, 2011); and Panabaj, Guatemala (Charbonnier et al., 2018). HCFs prevailed among lahar flows and deposits measured around Semeru, which provided characteristics similar to recent flows observed in Arequipa, such as the 8 February 2013 HCF (Ettinger et al., 2015).

We mapped scenario-based inundation zones and evaluated impacts on the building stock using simulation runs of real and potential mass flows obtained from the three numerical codes. Three scenarios for HCFs and DFs have been derived from the recorded small-to-moderate events with 1– 1.5×10^5 m^3 (e.g., the 8 February 2013 HCF) and moderate-to-large historical lahars (c. 2.5 m^3– 3.5×10^5 m^3 to 5×10^5 m^3).

6.2 Simulations Using Titan2F

Titan2F was developed at SUNY University at Buffalo for the modeling of biphasic (sediment-water) gravity-driven flows. The Titan2F model uses a similar framework to that developed by Pitman and Le (2005) for Titan2D. However, Titan2F has a complete set model of equations for both the granular phase and fluid phase (Córdoba et al., 2015; Córdoba et al., 2018). Titan2F is based on a depth-averaged, shallow layer model, as the fluid phase of the flow is modeled using a typical shallow water layer approach, while the frictional behavior of the solid phase is accounted for during the propagation of the simulated flow by assuming the Mohr–Coulomb model (Savage and Hutter, 1989).

6.2.1 Input and Output Parameters for Titan2F

In order to simulate sediment-water flows using Titan2F, a limited number of input parameters is required: 1) initial location and volume of the pile of debris, which collapses by gravity only upstream of the drainage channel that conveys flows; 2) initial solid concentration; 3) simulation time; and 4) volume (**Table 8**). Volumes ranging from 1.5 to 5×10^5 m^3 correspond to flow volumes derived from past and recent inundation areas within the city, geological mapping of lahar deposits in El Misti's drainage network, previous modeling obtained with LAHARZ (Delaite et al., 2005) and Titan2D codes (Vargas-Franco et al., 2010; Martelli, 2011; Pierson, 2005). Internal and basal friction angles vary during the flow propagation according to the variable solid concentration (Córdoba et al., 2015; Córdoba et al., 2018). The range of basal friction angles was 8°–18° in DFs simulated in Río Chili with Titan2D (Martelli, 2011). Internal friction angle ranges between 20° and 33° in simulations, lower than friction angles of the gravel- and sand-rich lahar deposits from El Misti (35°–38°, Pallares et al., 2015). The parameter of friction angles in lahar flows, as simulated with Titan2D, is directly incorporated in the Titan2F code, as the initial high frictions values of the Titan2F piles at the source decrease down valley according to the evolution of the solid concentration in time and space. If the solid concentrations become too low, the water-phase laws

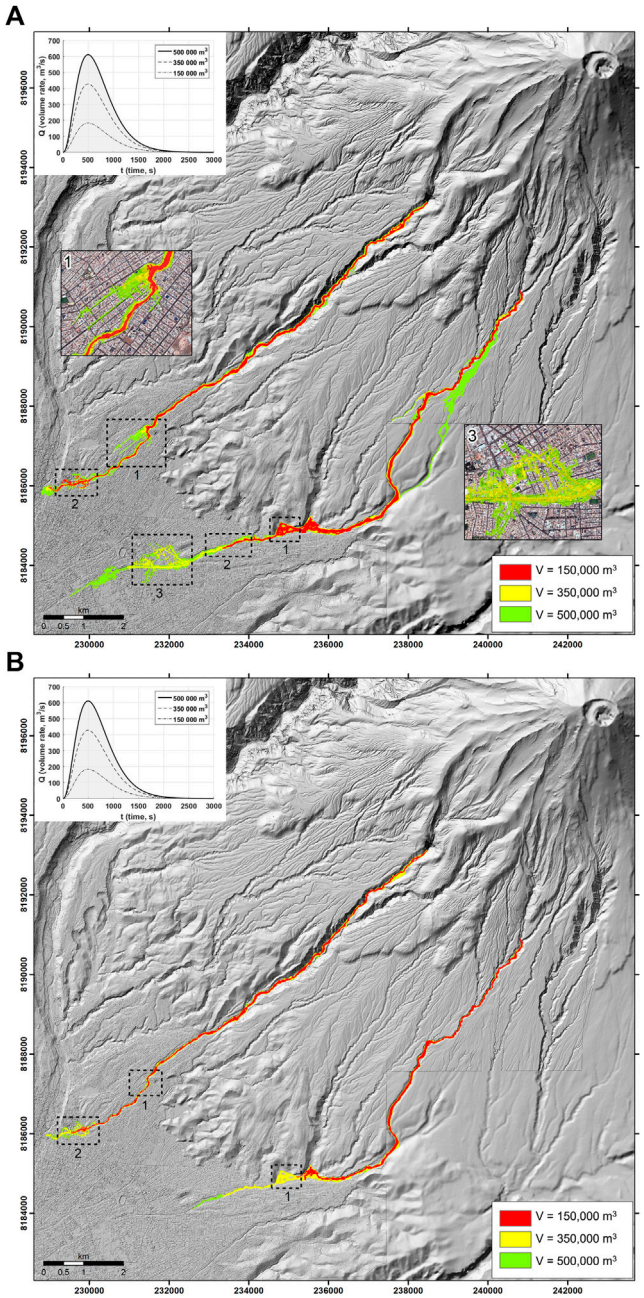

FIGURE 5 | VolcFlow simulation results using three HCF and DF scenarios with 0.15, 0.25, and 0.5 × 10^5 m^3 (**Table 8** for input and output parameters). Extent of simulated flows and overbank areas for HCF **(A)** and DF **(B)**. Dynamic pressure of HCF **(C)** and DF **(D)** in the middle reach of Qda. San Lazaro. Inset diagram shows the hydrograph used for three volumes of HCFs and DFs.

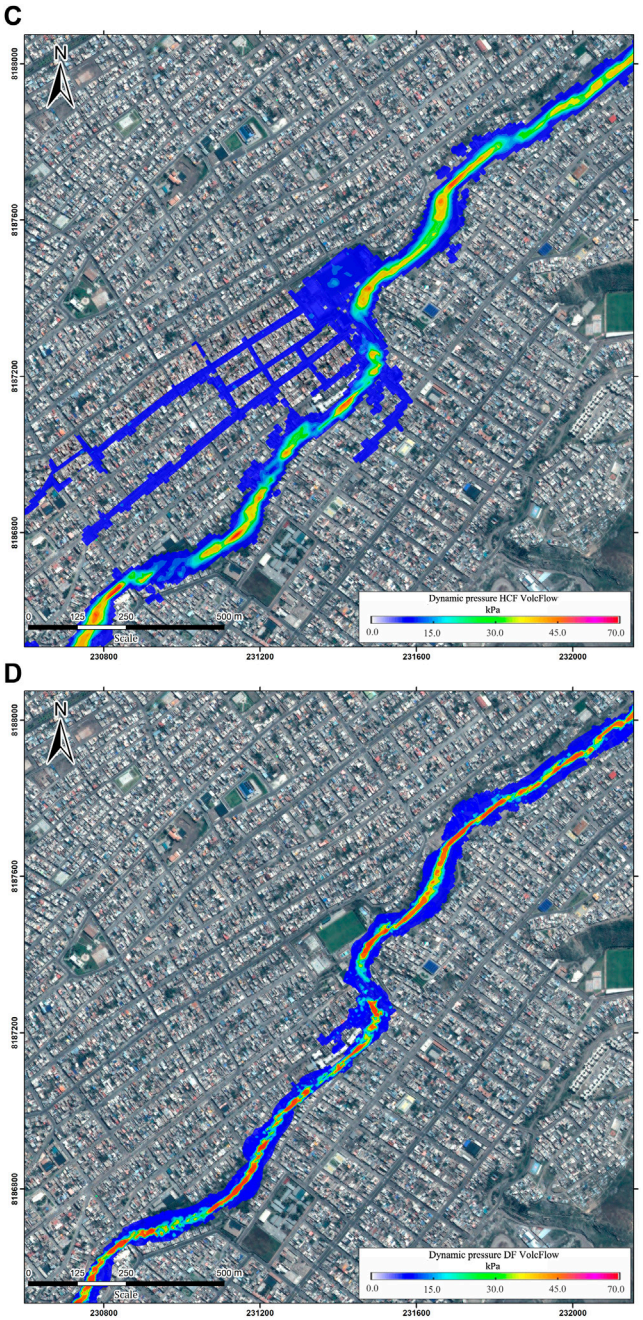

FIGURE 5a | *(Continued)*

become dominant over the friction-based solid phase (Córdoba et al., 2018).

Three scenarios (**Table 8**) were modeled using Titan2F with variable input parameters: three volumes, a duration of 240 min based on the database of flows observed in Arequipa (**Supplementary Table S1**), initial solid concentration typical of HCFs, and no initial velocity (**Table 8**). The worst-case scenario is assumed to result from the combination of the maximum volume (5 × 10^5 m^3) with the maximum solid concentration (30%–40% volume), based on large-scale historical lahars. Successive runs of three different volume flows were made on the DTM to delineate run-out zones and determine flow depth, velocity, and dynamic pressure.

Simulated flow depths and mean velocities are comparable with values observed in the 1915–2020 database and within the

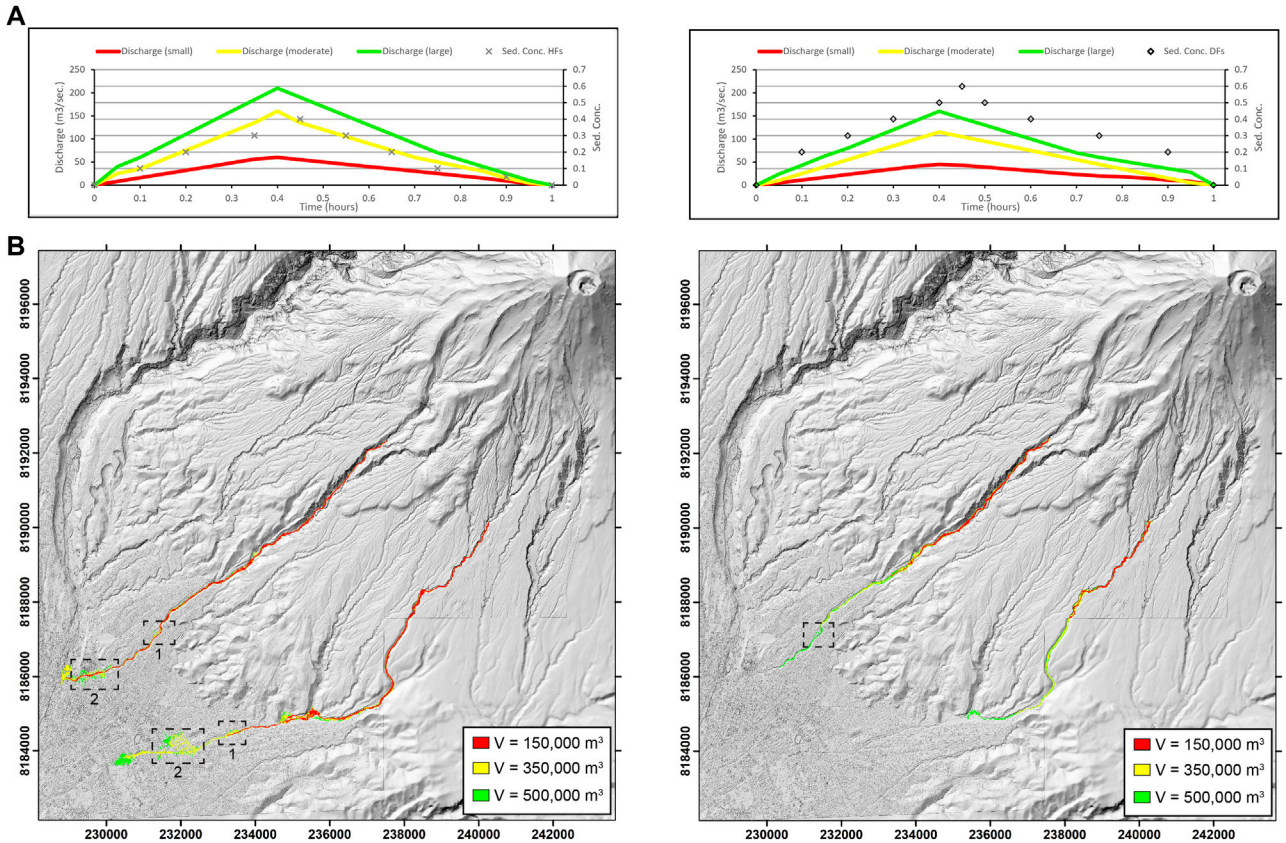

FIGURE 6 | FLO-2D simulation results for three HCFs (to the left-hand side) and three DFs (to the right-hand side) events in the San Lazaro and Huarangal catchments. **(A)** Inflow hydrographs for the three HCF and DF events considered: small-volume (red), moderate-volume (yellow), and large-volume (green). Sediment volumetric concentrations are also shown. **(B)**. Inundation map of the three simulated HCFs (left) and DFs (right). Dashed black rectangles and numbers show the major overbank areas along both catchments (see text for explanation).

low range of depth and velocity values reported in the aftermath of the 2013 HCF in the Qda. Venezuela. There, the velocity values were estimated based on equations of superelevation at channel bends (5.9–10.9 m; Ettinger et al., 2015). The mean velocity range of simulated flows remains comparable with the majority of HCFs and DFs measured in the Koboan–Lengkong River channels at Semeru (Doyle et al., 2010; Doyle et al., 2011), where rain-triggered, coarse-grained HCF pulses lasted for 1–3 h with heights of 0.5–2 m, peak velocities of 3–7 m/s, and discharges of 25–250 m^3/s.

Figures 4A,B show that simulated flows remain entrenched in ravine channels but spread out down valley in the dense urban area at the break in slope between the volcaniclastic fan and the Río Chili high terrace upstream of the historic center. Titan2F-based simulations did not show flow overbanks at sharp bends in the San Lazaro middle reach near the J. Olaya bridge with a moderate volume of 3.5×10^5 m^3 (**Figures 2A**, **4B**). Overbank areas, shown as rectangles 1–3 down valley (**Figures 4A,B**), correspond to sharp bends and change in slope in the ravine channel near el Golfo bridge, as well as damming and runup effects at the confluence with Río Chili. Despite wall containment 1.3 km upstream of the confluence with Río Chili, overbanks occur along Qda. San Lazaro due to the narrow channel capacity and constriction upstream of bridges. Along Qda. Huarangal-MM, the HCF and DF extent is more limited down valley: the 1.5×10^5-m^3 flow is restricted to the upper reach, while the $2.5–5 \times 10^5$-m^3 flows propagate to the middle reach only. Simulated overbanks also occur along the Qda. MM (Mariano Melgar) channels, which become narrower (10–20 m) and shallower (3–5 m) downstream of the bridge 8 de Octubre (**Figures 2B**, **4A**,**4B**). Noteworthy, the simulated flows spread out laterally upstream of that bridge onto two areas on the north side of the middle reach, coinciding with the inundated areas of the San Geronimo lahar in 2011.

Simulated dynamic pressure values along the San Lazaro channel (**Figure 4C**) show a range from 5 to 35 kPa with high (20–35 kPa) values concentrated in the middle of the channel. Dynamic pressure values of 20–25 kPa are significant on the channel edges and low terraces. Pressures as high as 35 kPa can cause significant damage to low-quality houses, and the most vulnerable building classes A0 and A are located on the adjacent low terraces (**Supplementary Figure S2**). Structural houses of types 1, 1A, 1B, and 2A, 2B on the channel edge can be destabilized and damaged by flows with modest (20 kPa) to high (35 kPa) dynamic pressure.

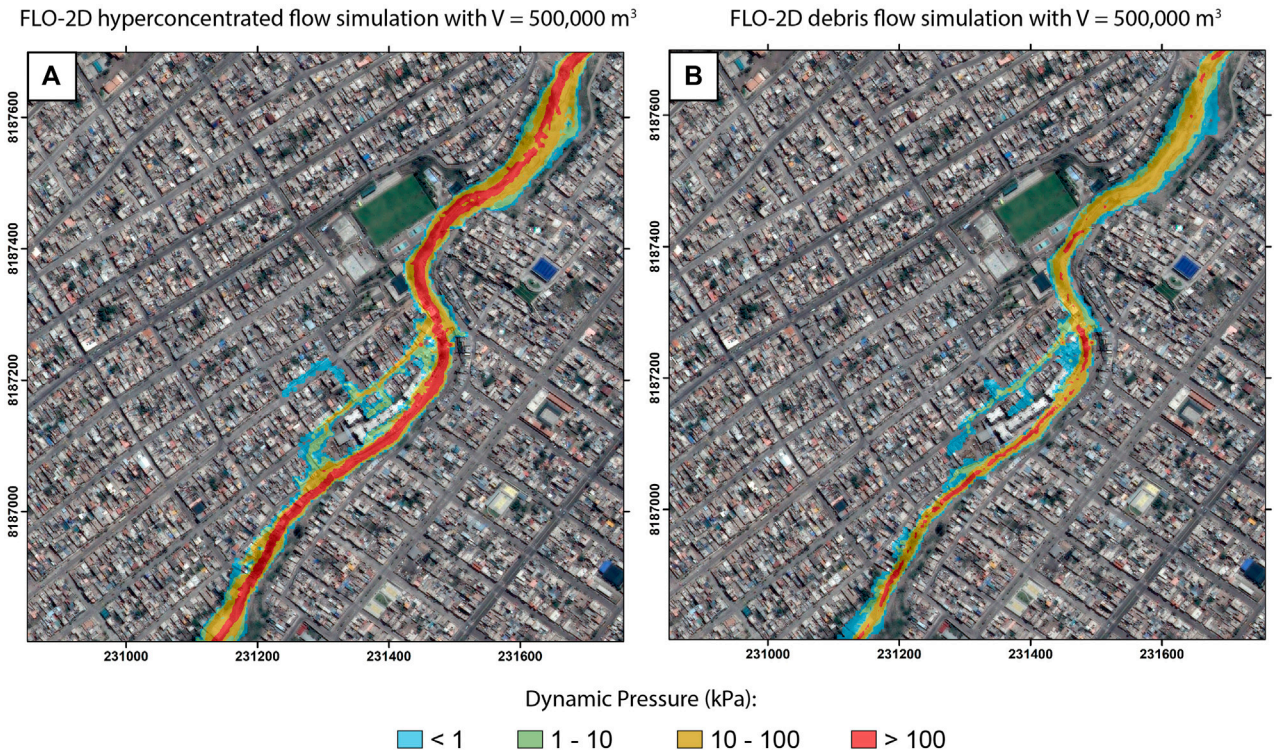

FIGURE 7 | Maps of simulated dynamic pressure (in kPa) obtained from FLO-2D simulations in a channel section (J. Olaya bridge linking the Miraflores and Alto San Alegre districts) of the San Lazaro catchment for **(A)** HCF and **(B)** DF, both with a volume of 5 × 10^5 m^3.

TABLE 9 | Input parameters used to simulate HCFs and DFs with VolcFlow numerical code and output parameters for three different scenarios. The parameter c is constant for all simulations and equals to 0.001.

Scenario		Input parameters					Output parameters		
		Volume *V*	Time	Density *ρ*	Yield strength τ_0	Viscosity *μ*	Flow depth *h*	Mean velocity *u*	Dynamic pressure *Pdy*
		×10^5 m^3	Min	kg/m^3	Pa	Pa.s	M	m/s	kPa
VF1	HCF	1.5	60	1,300	1	0	0.1–2.5	1.0–3.0	2.0–26.0
	DF	1.5	240	1900	100	10	0.2–2.5	1.0–3.4	2.0–26.0
VF2	HCF	2.5	60	1,400	20	1	0.3–3.5	1.0–5.2	2.0–31.0
	DF	3.5	240	2000	100	10	0.4–4	1.0–6.0	3.0–36.0
VF3	HCF	4.5	60	1,600	20	1	0.5–4.0	1.0–7.0	4.0–50.0
	DF	5.0	240	2,200	200	20	0.5–4.6	1.0–7.5	6.0–61.0

6.3 Simulations Using VolcFlow

VolcFlow was developed at the Laboratoire Magmas et Volcans to simulate the complex behavior of volcanic flows (Kelfoun and Druitt, 2005; Kelfoun et al., 2009; Kelfoun, 2017). It is based on the shallow water depth-averaged equations of mass and momentum balance, and the code allows the use of different rheological laws and source conditions. The equations are solved in a MATLAB® environment using a numerical method based on an Eulerian scheme by finite difference. The input parameters are the volume rate with time, and the flow is defined as a viscoplastic Bingham fluid (Rickenmann, 1991; Phillips and Davies, 1991; Julien and Lan, 1991; Major and Pierson, 1992) with a yield strength and viscosity (**Table 9**), combined with a turbulent-dispersive law that considers the effects of turbulence and dispersive stresses caused by sediment collisions. In the depth-averaged form, it is expressed as follows:

$$\boldsymbol{\tau} = \tau_0 \times \frac{\mathbf{u}}{\|\mathbf{u}\|} + 3 \times \mu \times \frac{\mathbf{u}}{h} + c \times \rho \times \mathbf{u} \times \|\mathbf{u}\|, \quad (1)$$

where τ_0 is the yield strength, μ is the viscosity, ρ is the flow density, h its thickness, and $\mathbf{u} = (u_x, u_y)$ its velocity. The coefficient c is a

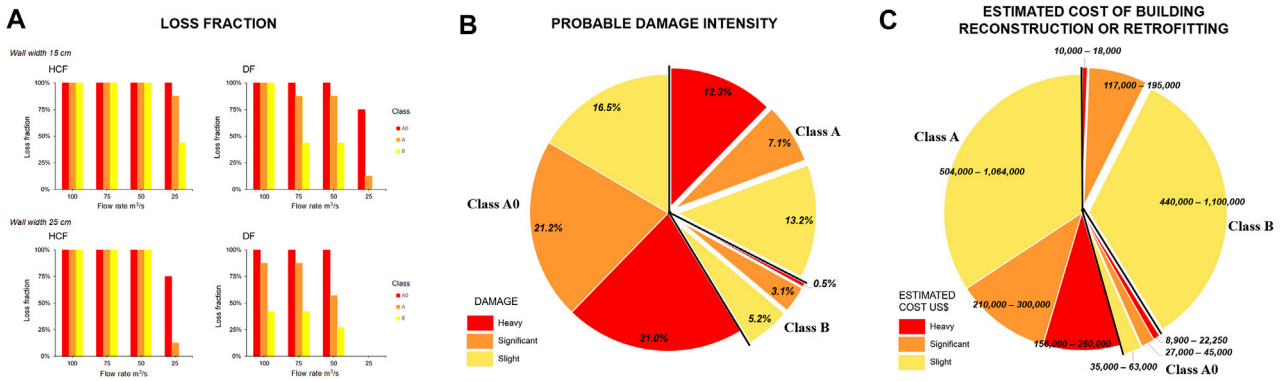

FIGURE 8 | (A) Loss fraction of buildings of classes A0, A, and B in case of DF and HCF for two wall widths of 15 and 25 cm (adapted and expanded from Mead et al., 2017). We expanded the 2017 study to all buildings located along both sides of both ravines under study within a distance of 50 m (maximum 100 m) from and an elevation of 5 m (maximum 10 m) above the channel. Numbers of buildings in class A0 = 249, class A = 138, and class B = 37. **(B)** Probable damage intensity considered three levels of damage: slight (impacts on walls, external elements, and roofs), significant (structural deficiency), and heavy (collapse) according to the location with respect to the channel and delineated area of dynamic pressure (**Figures 4C**, **5C**, **8**). Damaged buildings of class A0 (heavy 89, significant 90, slight 70); class A (heavy 55, significant 30, slight 53); and class B (heavy 2, significant 13, slight 22). **(C)** Estimated cost of reconstruction and/or retrofitting considered building classes A0, A, and B according to levels of damage. Cost is based on actual (2018–2019) construction value per m^2 in Arequipa but does not correspond to the commercial value based on age, location, maintenance of the building, and quality of the neighborhood.

dimensionless number that can be linked to the coefficient ξ of Voellmy ($c = \frac{g}{\xi}$) and that rules the turbulent dispersive pressure. The VolcFlow version used here is the single-phase version, in contrast to the two-phase regime used by Titan2F and FLO-2D codes.

Other input parameters used in VolcFlow are as follows (**Table 9**): 1) the same 4 m resolution DSM of the Arequipa area used for other codes and 2) an inflow hydrograph (inset, **Figures 5A,B**) imposed as a boundary condition and based on the measured rainfall amount and values of water and sediment discharge (yielding a flow volume). For this study, the volume rate Q of the hydrograph is approximated by the following law:

$$Q = k_1 \times t^{k_2} e^{-t/k_3}, \quad (2)$$

where $k_2 = 2.5$, $k_3 = 200$, and k_1 is computed to obtain the total flow volumes ranging from 1.5×10^5 m^3 to 5×10^5 m^3. Given these parameters, the volume rate increases to reach a peak discharge at 500 m^3/s and then decreases exponentially during ~2,000 s. The physical and rheological values, shown in **Table 9**, have been selected from empirical and experimental values calculated by Rickenmann (1991), Phillips and Davies (1991), Pierson (2005), Iverson et al. (2010), Iverson et al. (2011), and Manville et al. (2013).

Modeling scenarios were established for a set of HCFs and DFs in both Qda. San Lazaro and Huarangal (**Table 9**). In total, three scenarios, each including two types of mass flows, were defined for both ravines with a similar range of volumes ($1.5–5 \times 10^5$ m^3). We assume the worst-case scenario WF3 to be the result of maximum volumes (4.5 to 5×10^5 m^3) with a density of 2,200 kg/m^3, yield strength between 20 and 200 Pa, and viscosity between 1 and 20 Pas (**Table 9**). This scenario represents HCF and DF events triggered by heavy, durable rainstorm remobilizing abundant, loose material emplaced by post-eruptive lahars.

The results of numerical simulations corresponding to HCF showed a realistic extent of the impacted areas (**Figure 5A**) and reasonable values of velocity and flow depth compared to the observed flows from the database. However, overbanks were observed at the large bend, followed by channel constrictions near the J. Olaya bridge in the middle reach of Qda. San Lazaro (**Figure 2A**) when the hydrograph reaches a maximum flow rate of 500 m^3/s (inset **Figures 5A,B**).

The distribution of hydrodynamic pressures is between 35 and 100 kPa (**Figure 5C**) across the channel and low terraces 2–4 m high, where the most vulnerable houses (classes A0, A, and B) are located. For volumes in the order of $2.5–3.5 \times 10^5$ m^3, the large-volume scenario shows that major overbanks occurred from a sharp bend located just upstream of the José Olaya bridge and another just upstream El Progreso bridge (**Figures 2B**, **5B**).

6.4 Simulations Using FLO-2D

FLO-2D (FLO-2D Software Inc, 2021; O'Brien et al., 1993) is based on depth-averaged continuum flow equations. This code models lahar rheology using a shear stress relationship, and this rheology depends on the sediment concentration and flow mass, which vary during the flow propagation. Details about the code itself can be found in O'Brien et al. (1993), while the FLO-2D code was applied, for instance, by Charbonnier et al. (2018) to simulate the 2005 lahars at Panabaj (Guatemala). Two separate case studies are investigated here for the emplacement of 1) three DFs in the San Lazaro and Huarangal catchments and 2) three HCFs in the same catchments. The DFs and HCFs separately exhibited the same rheology and sediment concentration (i.e., all DFs were the same and all HCFs were the same). However, they each had three different volumes/discharges corresponding to small-, moderate-, and large-volume events.

FLO-2D includes various input parameters: 1) the DTM/DSM of the study area; 2) an inflow hydrograph based on measured rainfall accumulation and values of water and sediment discharge (i.e., flow volume); 3) a range of Manning roughness coefficients (0.03–0.08 according to the

channel geometry and material); 4) yield strength and dynamic viscosities expressed as a function of the volumetric sediment concentration:

$$\tau_y = \alpha_i e^{\beta i C v}, \quad (3)$$

$$\eta = \alpha_j e^{\beta j C v}, \quad (4)$$

where τ_y is the yield strength, η is the dynamic viscosity, C_v is the volumetric sediment concentration, and $\alpha_{i,j}$ and $\beta_{i,j}$ are two empirical coefficients obtained from O'Brien and Julien (1988) for HCFs and DFs with similar characteristics as the Misti ones; (5) the dimensionless laminar flow resistance K (**Table 7**); and (6) a Froude number, a dimensionless value defined as the ratio of kinetic energy to the potential energy that also accounts for the effect of gravity (**Table 7** for best-fit input values). Inflow hydrographs for each simulation are shown in **Figures 6A,B**. Peak discharge rates (water only) vary from 45–60 m^3/s (small-volume events) to 160–210 m^3/s (large-volume events) for both DF and HCF simulations, while peak sediment volumetric concentrations (attained after ~25 min) are set at 60 and 40 vol% for DF and HCF runs, respectively. Flow volumes vary between 1.5×10^5 m^3 (small-volume events) and 5×10^5 m^3 (large-volume events). Following Charbonnier et al. (2018), the Manning roughness coefficients vary with channel geometry and roughness between 0.03 and 0.08, the laminar flow resistance is set at 400, and the extended Froude number at 0.9 and two different rheological parameters ($\alpha_{i,j}$ and $\beta_{i,j}$) were used to simulate the differences in yield strengths and viscosities of DFs *versus* HCFs (**Table 7**). Inundation maps for the DFs and HCFs are shown in **Figures 6A,B**, respectively.

FLO-2D model results (**Figures 6A,B**) highlight the contrasting behavior of HCFs compared to DFs. Runout distances of the three simulated DFs (**Figure 6B**) do not exceed 16 km, and flows are confined to the main river channels only, except for a flow overspill that occurred in a sharp bend located just before the J. Olaya bridge (Miraflores district) in the Qda. San Lazaro (dashed black rectangle area in **Figure 6B**). In contrast, runout distances of the three simulated HCFs (**Figure 6A**) vary between 17 km (small-volume event) and >20 km (moderate-to-large-volume events), and major overspills from both sides of the San Lazaro and Huarangal-MM channels occurred between 15 and 20 km runout distances (dashed black rectangle areas in **Figures 6A,B**), with the moderate- and large-volume scenarios (volume $\geq 3.5 \times 10^5$ m^3) flooding the neighboring streets next to both Quebradas with <4 m thick water-rich HCFs. Along the San Lazaro channel section passing through the city of Arequipa, the major HCF overspills (up to 300 m in width) occurred at runout distances between 16.5 and 17.5 km (overbank area two in **Figure 6A**), in areas of channel constriction, first at the El Progreso bridge and in the Selva Alegre and Historic Center districts. Along the Huarangal-MM channel in Arequipa, a minor overspill (<130 m width) occurred first along an area of channel constriction due to the presence of the Tupac Amaru bridge (overbank area one in **Figure 6A**). Then, a major overspill occurred ~1 km downstream of the Santa Rosa bridge, flooding the streets on the NW area up to 800 m away from the Qda. Huarangal-MM (overbank area 2 in **Figure 6A**). Flow overspills located at the distal end of both Quebradas (before reaching the Río Chili in the San Lazaro and in the Explanada Dolores (a meeting square for public events) in the Huarangal-MM, are due to the poor resolution of the topography on the DSM in these areas, mostly due to the presence of trees.

These first FLO-2D modeling results at Misti highlight that while DFs are mostly confined in the main river channels, impacted areas of moderate-to-large-volume (>3.5×10^5 m^3) HCFs in the city of Arequipa can be extensive and dangerous. HCFs can spill over from the shallow and narrow riverbeds and inundate highly populated streets and critical city roads and bridges.

7 DISCUSSION

The numerical simulations show acceptable results as they can reproduce the extent of the areas impacted by mass flows from the 1915–2020 database. Three computational models used for evaluating the propagation of HCFs and DFs can delineate and forecast the potentially flooded and overbank areas.

7.1 Uncertainties and Limitations Linked to Simulations

Uncertainties and limitations associated with tephra-fall scenarios and modeling have already been addressed in Sandri et al. (2014). The authors considered the natural variability of the eruptive process in terms of eruptive sizes and vent location. Many possible scenarios were combined, each one weighted with its own probability of occurrence. This allowed the authors to quantify how the uncertainty in the eruptive size and vent location affected the probability for different areas around the volcano to be impacted in a given time window: the associated hazard. Herein, uncertainties are linked to the choice of two hazard metrics: the tephra load of 100 and 250 kg/m^2. The first choice was driven by the poor-to-moderate resistance of the majority of the roofs in the surveyed neighborhoods along the San Lazaro ravine. The majority of flat roofs and the paucity of pitched roofs across Arequipa reduces the roof resistance. As the probability of ashfall toward the city increases during the rainy season, one of the study limitations stems from the fact that the rainfall was not included in the tephra-fall scenario. Wet tephra will have a considerable effect on the metal sheet and hybrid roofs if the latter are not cleaned during the eruption.

Input parameters of the three numerical codes cannot be used for benchmarking purposes. However, we can compare outputs (extent, paths, overbank areas, velocity, and flow depth) with characteristics reported from the most recent flow events. All three codes did a good job in reproducing observed flows, particularly recent HCFs across two basin ranges in Arequipa, which are the most common events from the database 1915–2020. Simulation runs show the expected path and

extent along the entrenched ravine channels, particularly Qda. San Lazaro. All runs show overbank areas down valley at sharp bends, break in slope between volcaniclastic fans, and upstream of narrow bridges. In the Qda. Huarangal-MM, the most voluminous DFs and HCFs only can reach the densely populated neighborhoods along the middle and lower reaches. This is due to the long (16 km) path and gentle slope down valley, and Titan2F simulated flows are shorter than other flows simulated with VolcFlow and FLO-2D. The shorter inundated areas may be due to at least three factors: 1) the Mohr–Coulomb model prevents the flow from propagating on slopes below the lowest basal friction angles chosen as input; 2) viscosity, allowing the flow to propagate on gentle slopes, is not considered in Titan2F; and 3) the initiation process is not a mass flux, but a pile of material which collapses due to gravity.

Titan2F-simulated flows display a narrow extent, shorter paths, particularly in the Qda. Huarangal-MM, and a limited number of overbanks with respect to documented channel sinuosity and constrictions. VolcFlow- and FLO-2D-simulated flows exhibit longer and/or wider paths, higher velocity, and overbanks in the same areas at bends and down valley, which pinpoint reaches where attention must be drawn for mitigation measures to be implemented (containment wall, check dams, or enlargement of bridges). VolcFlow and FLO-2D reproduce overbank at the Olaya bridge bend in the middle reach of San Lazaro that does not appear with Titan2F runs.

The outputs of all three codes included flow depth, velocities, and dynamic pressure. Ranges of flow depth (0.1–4.6 m) and velocities (1–9 m/s) are comparable between codes and real flows and with simulated flows in the literature, whereas the distribution of dynamic pressure differs between the code outputs. Dynamic pressure has never been measured during or immediately after flows in Arequipa. By considering the same middle reach of the Qda. San Lazaro, the range of dynamic pressure is narrower with Titan2F runs (0–50 kPa), widens to 75 kPa with VolcFlow runs, and expands beyond 100 kPa with FLO-2D runs. VolcFlow- and FLO-2F-simulated HCF and DF display a wider area impacted by dynamic pressure on both sides of the ravine channel, extending onto the low terraces or banks on which low-quality buildings are located (**Figures 5C**, **7**). Usually, HCFs exert a weaker dynamic pressure range than DFs, but FLO-2D-simulated HCFs show a higher dynamic pressure range (**Figure 7**).

By using FLO-2D, density is automatically computed according to the specific weight of the flow, which varies progressively as the flow propagates down valley. Density values can be much higher in HCFs than DFs in channels; in contrast, density is an initial parameter within Titan2F and VolcFlow and does not change down valley. In terms of rheology, HCFs mostly displayed the highest dynamic pressures acting on parallel walls (Mead et al., 2017). The higher density (compared to Newtonian flows) is responsible for the larger dynamic pressures (Jenkins et al., 2015). This effect is moderated by the yield strength of HCFs, causing the velocity to be lower than Newtonian flows near perpendicular walls. DF pressures are much lower than both Newtonian and HCFs as the yield strength and dilatant rheology components limit overbank flow velocities.

From estimated values of lahar impact pressure in Sarno, Italy, Zanchetta et al. (2004) argued that the complete destruction of a building required a pressure exceeding 90 kPa. Below this value, structures were generally heavily (35–90 kPa) or moderately (<35 kPa) damaged. The required pressure to break a large single-glazed window was as low as 1–2 kPa, and it was little more than 3 kPa for a wooden door. Therefore, an important point is that openings are the weakest points of buildings and are a critical parameter to quantify in buildings surveys. The dynamic pressure threshold of 35 kPa (Zanchetta et al., 2004) for moderate damage would be the case along both ravines for flows simulated with Titan2F and VolcFlow. The dynamic pressure threshold of 90 kPa for severe damage has been reached along both channels, as shown by HCFs and DFs simulated with FLO-2D. Heavy damage triggered by dynamic pressure between 35 and 90 kPa can be attained in the channel center and along sharp curves and/or narrow sections (e.g., upstream and near the J Olaya bridge; **Figures 5C**, **7**). In all cases, the high (30%–50%) proportion of openings, the prevailing single-glazed windows in surveyed buildings in Arequipa, represent the weakest point for HCF and DF impacts in Arequipa.

7.2 Impacts of Tephra Fall on Roofs

The evaluation of tephra load on roofs has shown that at least 50% of building roofs of classes A0, A, and B are highly vulnerable to tephra load of 250 kg/m^2, a force of 2 kN/m^2. This is equivalent to a 10-cm-thick tephra that would fall in the rainy season over the city. As future El Misti eruptions would likely produce 10- to 50-cm-thick tephra-fall deposits, the probabilities of roof collapse would affect at least four among the nine categories of roofs.

Considering the cost of roof collapse, the low quality of roofs, and the low-income households in the surveyed neighborhoods, retrofitting and construction need to be undertaken by the municipality, the regional government, and NGOs. Specific construction rules and prevention procedures should be implemented as soon as El Misti awakens and before an imminent eruption.

7.3 Impacts of Mass Flows on Habitat and Loss Evaluation

Damage from water-rich flows is induced by a combination of three principal forces: 1) hydrodynamic pressure, 2) hydrostatic pressure, and 3) the collisional force of boulders (Thouret et al., 2020, and references therein). Hydrodynamic pressure exerted by the flow front/head, having horizontal and vertical components, is the kinetic energy per unit volume of the flow, which changes with flow density. Hydrostatic pressure depends on the depth and weight of the wet flow until it solidifies and acts toward the end of the event once the deposit is stabilized. Herein, we will not consider boulders, which act like missiles, hitting structures, and obstacles. Hydrodynamic pressure is proportional to the square of the frontal velocity as follows:

$$Pdy = k\rho d f v^2, \tag{5}$$

where Pdy is the dynamic pressure; k is a constant, which depends on the density of the granular material, flow dynamics, and flow

homogeneity and constituents; ρdf is the mean density of the mixture; and v is the velocity of the flow front.

Zeng et al. (2015) distinguished three principal damage categories for reinforced concrete and masonry structures by linking flow processes with hazard intensity: 1) inundation or burial, including damage to the ground floor or external walls of a building together with debris entering rooms, but without significant damage to structural components; 2) serious structural damage owing to flow front impact or boulder impacts triggering the failure of single structural elements, or the collapse of the whole structure; and 3) undercutting where soil erosion and/or liquefaction deforms foundations and subsequently buildings tilt or collapse. Faella and Nigro (2003) and Nigro and Faella (2008) stated that the severity of LH/DF impacts largely depended on the orientation and structural types of edifices and the kinetic energy of flows (a function of velocity, density, and Froude number).

From the evaluation of fragility curves by Mead et al. (2017) in the Qda. Dahlia, a tributary of Qda. Huarangal, we elaborated fragility curves for 425 buildings surveyed in 2018 and 2019 along the Qda San Lazaro and Huarangal. Fragility curves (**Supplementary Figure S4** taken from Mead et al., 2017) were adapted and expanded to all surveyed buildings of classes A0, A, and B along both quebradas. Fragility curves based on hydrodynamic pressure and flow depth indicate to which extent buildings of classes A0, A, and B with wall bricks of 25 and 15 cm width would be affected by the ultimate bending moment before collapsing. The ultimate bending moment

$$Mu = (ft + fd)wb2/6, \tag{6}$$

where ft is the tensile strength of the masonry wall, fd is the design compressive stress acting on the wall, w is the width of the wall facing the flow, and b is the thickness of the wall.

Brick walls (and "bloquetas," i.e., lapilli-rich rubble stones) represent about 60% of the buildings in these areas. **Figures 5C**, **7** and **Supplementary Figure S4** suggest that moderate dynamic pressure in the range of 20–30 kPa and flow depth <1.5 m would suffice to bend the 15-cm-thick and 25-cm-thick brick walls, respectively.

Figure 8A, adapted and expanded from Mead et al. (2017), shows the loss fractions of buildings having brick walls (15 and 25 cm thick, respectively) due to HCF and DF with flow rates as low as 25–100 m^3/s. Three out of four flow rate values (25, 50, and 75 m^3/s) considered in the loss evaluation of buildings of classes A0, A, and B correspond to the 5- to 10-year return period of flow events in Arequipa (**Table 6**), to be compared with flow rates in the order of 125 m^3/s during the 8 February 2013 HCF in Qda. Venezuela, which represents a 50-year return period flow according to **Table 6**. The loss proportion of all class buildings is 30% higher for the brick wall of 15 cm thickness when HCFs are considered with respect to DFs. For the 15-cm-thick brick walls, the loss proportion of class A0 buildings is high (75%–100%) in all HCF and DF cases, the loss proportion of class A buildings is relatively high (85%–100%) in case of HCF but less in case of DF (10–85%). The loss is relatively minor (0%–40%) for class B buildings in case of DF except for flow rates ≥100 m^3/s and substantial (45%–100%) in case of HCF. As a result, a substantial loss of low-quality buildings on both sides of the ravines in Arequipa would result from HCFs within the range of 5- to 10-year return period of low-to-moderate (25–75 m^3/s) flow rates.

7.4. Toward an Assessment of Monetary Cost

The monetary cost of loss fractions of buildings has been estimated according to flow scenarios to contribute to planning emergency procedures and civil defense works. The range of cost has been estimated for each structural type of building (**Table 3**; **Figure 8C**). Evaluating cost is challenging in Arequipa because financial issues are a sensitive subject, particularly in city suburbs, where the declaration of assets is biased and tax evasion is omnipresent. **Figure 8C** displays the estimated cost range of construction/retrofitting of each building type, which is not the market value, depending on construction age and location, use, maintenance, and other factors. The estimated cost range (**Figure 8C**) is based on damage level proportions of building classes (**Figure 8B**). Class A0 buildings show the highest (16%–21%) damage levels in all categories (heavy, significant, and slight). Class A buildings display moderate (7%–13%) damage levels in almost all categories, while class B buildings exhibit low (0.5%–5%) damage levels. In terms of monetary cost, the situation is the opposite, as the most vulnerable class is low quality and "cheap" housing. Thus, the estimated cost of reconstruction or retrofitting of damaged class A0 buildings is quite low (0.7%–2.2%). The estimated cost of damaged class A buildings is moderate to substantial (9.7%–32.9%), while the cost of less damaged but regular-quality class B buildings covers a wide range between low (0.6%) and high values (34.1%), which is explained by the fact that a small proportion (<5%) of class B buildings would suffer severe or significant damage.

Should a prevention policy be implemented in the near future, we suggest that houses of classes A0 and A bordering the ravines could be relocated on high terraces at a minimum distance of 250 m away from the channel. Alternatively, the financial and logistical support of the Municipality, Regional Government, Ministry of Housing, and NGOs would allow the reconstruction of houses of classes A0 and A, for example, in the SE basin of Arequipa away from the ravines and El Misti (Municipalidad Provincial de Arequipa, 2011). A large proportion of severely and significantly damaged class A buildings should be reconstructed, while the slightly damaged proportion should be retrofitted. Class B buildings, probably slightly damaged in small proportion, can be retrofitted. Wall containment at sharp bends and enlargement of bridge arches in constricted channels are recommended where overbank flows were simulated and actually occurred in the past.

CONCLUDING REMARKS

The work presented here has assessed the impacts of potential tephra fall and recent mass flows along two ravines that cross the city of Arequipa.

1) The evaluation of tephra load on roofs has shown that a substantial 11%–38% of low-quality and hybrid roofs

would be severely affected when considering the lowest hazard metrics (100 kg/m^2, i.e., 1 kN). This corresponds to the low magnitude/moderate frequency scenario, involving a tephra-fall deposit at least 10 cm thick over the city in the rainy season. The high probability of roof collapse in case of modest eruptions, such as the mid-15th-century event, combined with rainfall may press decision-makers to undertake roof retrofitting and include risk policy in urban planning.

2) Titan2F, VolcFlow, and FLO-2D models helped delineate and forecast the potentially dangerous inundation and overbank areas from a set of HCFs and DFs with flow volumes from 1.5 to 5×10^5 m^3 based on a database of flow events over the past 105 years and on historical lahars.
3) Simulated flow paths, extents, flow depths, and velocities range between values of recent flows and older events described in the literature. Impacts are measured by estimating the dynamic pressure of the simulated flows, which differ from code to code. Substantial damage would include vulnerable buildings near the channel in highly populated suburbs along drainage basins. Buildings of classes A0 and A with brick walls would be severely damaged by HCFs, particularly with flow rates below 100 m^3/s.
4) Loss fraction of buildings would be 30% in case of HCFs with 5- to 10-year return period discharges, and the proportion would increase to 100% of the lowest-quality houses hosting the most vulnerable inhabitants near the ravine channels. The cost of reconstruction and retrofitting, which would be necessary for all class A0 buildings and a sizeable proportion of class A buildings, may be unbearable for the local population. This requires attention from the civil authorities at both regional and national levels.
5) Results are potentially usable for urban planning in Arequipa. Applying the proposed methodology for assessing impacts due to HCFs and DFs is useful to understand the extent of mass-flow impacts during significant rainstorm events and develop emergency plans. This, in turn, helps raise awareness among local inhabitants and helps stakeholders formulate adequate disaster management policies in Peru or Latin American cities exhibiting similar disaster-prone conditions.

DATA AVAILABILITY STATEMENT

The original contributions presented in the study are included in the article/**Supplementary Material**, further inquiries can be directed to the corresponding authors.

AUTHOR CONTRIBUTIONS

EA: field surveys, simulations using numerical code Titan2F and VolcFlow, and writing. J-CT: research project design, data collection, field surveys, and writing 50%. AG: field surveys, roof vulnerability, and writing. DR: field surveys and numerical code Titan2F. SC: simulations using numerical code FLO-2D and writing. KK: simulations using numerical code VolcFlow. GC: field survey and Titan2F training for co-authors. OS: GIS and mapping.

FUNDING

Fieldwork and laboratory analyses have been funded by the French government IDEX-ISITE initiative 16-IDEX-0001 CAP 20-25.

ACKNOWLEDGMENTS

The first authors thank the Institut de Recherche pour le Développement (IRD) for constant logistical support in Peru. The second author has been bestowed two travel grants from IRD that enabled her to work at LMV-UCA in 2019 and 2021. We thank our Peruvian colleagues and students from INGEMMET, IGP, and UNSA (in particular J. Mariño, M. Rivera, and F. Garcia), and INDECI as well (GA. Arguedas, J. Vasquez, H. Pareja) for their support over the years and kindly sharing their ideas about hazards and risk in the city of Arequipa.

SUPPLEMENTARY MATERIAL

The Supplementary Material for this article can be found online at: https://www.frontiersin.org/articles/10.3389/feart.2022.865989/full#supplementary-material

REFERENCES

Aguilar Contreras, R., Taipe Maquerhua, E., Antayhua Vera, Y., Ortega Gonzáles, M., Apaza Choquehuayta, F., and Cruz Mamani, M. (2022). Hazard Assessment Studies and Multiparametric Volcano Monitoring Developed by the Instituto Geológico, Minero Y Metalúrgico in Peru. *Volcanica* 4 (S1), 73–82. doi:10.30909/vol.04.S1.7392

Aguilar, Z., Ronca, M., and Piedra, R. (2017). "Probabilistic Seismic hazard Assessment in the Peruvian Territory," in 16th World Conference on Earthquake, 16WCEE Santiago Chile, 9-13 January 2017, 10. Paper no. 3028.

Alves, B. (2021). *Natural Disasters in Latin America– Statistics and Facts. Statista Report*. Hamburg, Germany: Statista GmbH.

Arapa, E. (2019). *Hazards, Physical Vulnerability and Simulations of Impacts from Mass Flows (Lahars) and Flash Floods in the City of Arequipa, Peru. (Unpubl.) Report*. Lima: Université Clermont-Auvergne and UNSA Arequipa, IGP, 48.

Bardou, E., Bowen, P., and BoivinBanfil, P. P. (2007). Impact of Small Amounts of Swelling Clays on the Physical Properties of Debris-flow-like Granular Materials. Implications for the Study of alpine Debris Flows. *Earth Surf. Proc. Landf.* 32, 5 698–710. doi:10.1002/esp.1412

Beverage, J. P., and Culbertson, J. K. (1964). Hyperconcentrations of Suspended Sediment. *J. Hydr. Div.* 90, 117–128. doi:10.1061/jyceaj.0001128

Blong, R. J., Grasso, P., Jenkins, S., Magill, C. R., Wilson, T. M., McMullan, K., et al. (2017). Estimating Building Vulnerability to Volcanic Ashfall for Insurance and Other Purposes. *J. Appl. Volcanol.* 6 (1), 1–13. doi:10.1186/s13617-017-0054-9

Cesca, M., and D'Agostino, V. (2008). Comparison between FLO-2D and RAMMS in Debris-Flow Modelling: a Case Study in the Dolomites. Monitoring, Simulation, Prevention and Remediation of Dense Debris Flows II. *WIT Trans. Eng. Sci.* 60, 197–206. doi:10.2495/DEB080201

Charbonnier, S. J., Connor, C. B., Connor, L. J., Sheridan, M. F., Oliva Hernández, J. P., and Richardson, J. A. (2018). Modeling the October 2005 Lahars at Panabaj (Guatemala). *Bull. Volcanol.* 80, 4. doi:10.1007/s00445-017-1169-x

Charbonnier, S. J., Thouret, J. C., Gueugnon, V., and Constantinescu, R. (2020). New Insights into the c.2070 Cal Yr BP Pyroclastic Currents at El Misti Volcano (Peru) from Field Investigations, Satellite Imagery and Probabilistic Modeling. *Front. Earth Sci.* 8, 557788. doi:10.3389/feart.2020.557788

Chávez, J. A. (1992). La erupción del Misti. Pasado, presente, futuro. *Arequipa: Impresiones Zenith*, 178. doi:10.2172/5420913

Chehade, R. (2021). *Développement d'un modèle numérique d'impact pour la quantification de la vulnérabilité du bâti exposé aux coulées de débris et crues éclair*. Clermont-Ferrand: Université Clermont-Auvergne, Sciences pour l'Ingénieur, Polytech-Génie Civil, 165.

Cobeñas, G., Thouret, J.-C., Bonadonna, C., and Boivin, P. (2012). The c.2030 Yr BP Plinian Eruption of El Misti Volcano, Peru: Eruption Dynamics and hazard Implications. *J. Volc Geoth Res.* 241-242, 105–120. doi:10.1016/j.jvolgeores.2012.06.006

Cobeñas, G., Thouret, J. C., Bonadonna, C., , et al.Thouret, J.-C., Bonadonna, C., Boivin, P. (2014). Reply to Comment on: "CobeñasThe c.2030 Yr BP Plinian Eruption of El Misti Volcano, Peru: Eruption Dynamics and hazard Implications. *J. Volc Geoth Res.* 275C, 103–113. doi:10.1016/j.jvolgeores.2014.02.014

Connor, L., and Connor, C. (2011). *Tephra2D Users Manual*. vhub: Open source software, 33.

Córdoba, G., Villarosa, G., Sheridan, M. F., Viramonte, J. G., Beigt, D., and Salmuni, G. (2015). Secondary lahar hazard assessment for Villa la Angostura, Argentina, using Two-Phase-Titan modelling code during 2011 Cordón Caulle eruption. *Nat. Haz. Earth Syst. Sci.* 15 (4), 757–766. doi:10.5194/nhess-15-757-2015

Córdoba, G. A., Sheridan, M. F., and Pitman, B. E. (2018). Titan2F Code for Lahar hazard Assessment: Derivation, Validation and Verification. *Rev. Soc. Geol. Mexic.* 70 (3), 611–631. doi:10.18268/BSGM2018v70n3a3

Delaite, G., Thouret, J.-C., Sheridan, M., Labazuy, Ph., Stinton, A., Souriot, T., et al. (2005). Assessment of Volcanic Hazards of El Misti and in the City of Arequipa, Peru, Based on GIS and Simulations, with Emphasis on Lahars. *Zeitschrift für Geomorphol. Suppl. Iss.* 140, 209–231.

Doyle, E. E., Cronin, S. J., Cole, S. E., and Thouret, J.-C. (2010). The Coalescence and Organization of Lahars at Semeru Volcano, Indonesia. *Bull. Volcanol* 72 (8), 961–970. doi:10.1007/s00445-010-0381-8

Doyle, E. E., Cronin, S. J., and Thouret, J. C. (2011). Defining Conditions for Bulking and Debulking in Lahars. *Geol. Soc. America Bull.* 123, 1234–1246. doi:10.1130/b30227.1

Dumaisnil, C., Thouret, J.-C., Chambon, G., Doyle, E. E., Cronin, S. J., and Surono, M. (2010). Hydraulic, Physical and Rheological Characteristics of Rain-Triggered Lahars at Semeru Volcano, Indonesia. *Earth Surf. Process. Landforms* 35, 1573–1590. doi:10.1002/esp.2003

Ettinger, S., Mounaud, L., Magill, C., Yao-Lafourcade, A.-F., Thouret, J.-C., Manville, V., et al. (2015). Building Vulnerability to Hydro-Geomorphic Hazards: Estimating Damage Probability from Qualitative Vulnerability Assessment Using Logistic Regression. *J. Hydrol.* 541, 563–581. doi:10.1016/j.jhydrol.2015.04.017

Faella, C., and Nigro, E. (2003). "Dynamic Impact of the Debris Flows on the Construction during the Hydrogeological Disaster in Campania 1998: 1. Description and Analysis of the Damage, 2. Failure Mechanical Models and Evaluation of Impact Velocity," in *Proc. Int. Conf. 'Fast Slope Movement Prediction and Prevention for Risk Mitigation'*. Editor L. Picarelli (Bologna: Patron).

Fernandez-Davila, J., and Benites Montufar, A. (2003). *Inundaciones en la localidad de Arequipa ocasionadas por el ingreso de las torrenteras*. Arequipa: UNSA Universidad San Agustin de Arequipa, Instituto Geofisico de Characato Unpubl. Report, 51.

FLO-2D Software Inc (2021). FLO-2D ProModel. Available at: https://www.flo-2d.com/.

Freitas Guimarães, L., Nieto-Torres, A., Bonadonna, C., and Frischknecht, C. (2021). A New Inclusive Volcanic Risk Ranking, Part 2: Application to Latin America. *Front. Earth Sci.* 9, 757742. doi:10.3389/feart.2021.757742

Fuse, J., and Benites, A. (2003). "Estudio: inundaciones en la localidad de Arequipa ocasionadas por el ingreso de las torrenteras," in *Universidad Nacional San Agustin (UNSA) internal (Unpubl.) research report* (Arequipa), 51.

George, D. L., and Iverson, R. M. (2014). A Depth-Averaged Debris-Flow Model that Includes the Effects of Evolving Dilatancy. II. Numerical Predictions and Experimental Tests. *Proc. R. Soc. A.* 470, 20130820. doi:10.1098/rspa.2013.0820

Gutiérrez, R. (1992). *Evolución Histórica Urbana de Arequipa 1540-1990*. Primera ed. Lima: Epígrafe Editores.

Harpel, C., da Silva, S., Salas, G., Cobeñas, G., Thouret, J.-C., Bonadonna, C., et al. (2013). Comment onThe c.2030 Yr BP Plinian Eruption of El Misti Volcano, Peru: Eruption Dynamics and hazard Implications. *J. Volcanol. Geoth. Resj Volcanol Geoth Res.* 275, 103–113. doi:10.1016/j.jvolgeores.2014.02.014

Harpel, C. J., de Silva, S., and Salas, G. (2011). The 2 Ka Eruption of Misti Volcano, Southern Peru-The Most Recent Plinian Eruption of Arequipa's Iconic Volcano. *Geol. Soc. Am. Spec. Pap.* 484, 72. doi:10.1130/2011.2484

Hungr, O., and Jakob, M. (2005). *Debris Flows Hazards and Related Phenomena*. Praxis: Springer, 728.

INDECI (2019). *Compendio Estadístico de Emergencias para el periodo 1995-2019*. Lima: Instituto Nacional de Defensa Civil.

INEI (2018). *Resultados definitivos de los Censos Nacionales 2017 - Arequipa (XII de población, VII de vivienda y III de comunidades indígenas)*. Lima: Instituto Nacional de Estadística e Informática, 641.

Iverson, R. (2005). "Debris-flow Mechanics," in *Debris Flow Hazards and Related Phenomena*. Editors M. Jakob and O. Hungr (Heidelberg: Springer-Praxis), 105–134.

Iverson, R. M. (2014). Debris Flows: Behaviour and hazard Assessment. *Geology. Today* 30 (1), 15–20. doi:10.1111/gto.12037

Iverson, R. M., Logan, M., LaHusen, R. G., and Berti, M. (2010). The Perfect Debris Flow? Aggregated Results from 28 Large-Scale Experiments. *J. Geophys. Res.* 115, F03005. doi:10.1029/2009JF001514.29

Iverson, R. M., Reid, M. E., Logan, M., LaHusen, R. G., Godt, J. W., and Griswold, J. P. (2011). Positive Feedback and Momentum Growth during Debris-Flow Entrainment of Wet Bed Sediment. *Nat. Geosci* 4 (2), 116–121. doi:10.1038/ngeo1040

Iverson, R. M. (1997). The Physics of Debris Flows. *Rev. Geophys.* 35 (3), 245–296. doi:10.1029/97rg00426

Jenkins, S. F., Phillips, J. C., Price, R., Feloy, K., Baxter, P. J., Hadmoko, D. S., et al. (2015). Developing Building-Damage Scales for Lahars: Application to Merapi Volcano, Indonesia. *Bull. Volcanol* 77 (9), 1–17. doi:10.1007/s00445-015-0961-8

Julien, P. Y., and Lan, Y. (1991). Rheology of Hyperconcentrations. *J. Hydraulic Eng.* 117, 346–353. doi:10.1061/(asce)0733-9429(1991)117:3(346)

Kelfoun, K. (2017). A Two-Layer Depth-Averaged Model for Both the Dilute and the Concentrated Parts of Pyroclastic Currents. *J. Geophys. Res. Solid Earth* 122, 1–19. doi:10.1002/2017jb014013

Kelfoun, K., and Druitt, T. (2005). Numerical Modeling of the Emplacement of Socompa Rock Avalanche, Chile. *J. Geophys. Res.* 110, B12202–B12202. doi:10.1029/2005jb003758

Kelfoun, K., Samaniego, P., Palacios, P., and Barba, D. (2009). Testing the Suitability of Frictional Behaviour for Pyroclastic Flow Simulation by Comparison with a Well-Constrained Eruption at Tungurahua Volcano (Ecuador). *Bull. Volcanol.* 71 (9), 1057–1075. doi:10.1007/s00445-009-0286-6

Lavigne, F., and Thouret, J.-C. (2003). Sediment Transportation and Deposition by Rain-Triggered Lahars at Merapi Volcano, central Java, Indonesia. *Geomorph* 49 (1-2), 45–69. doi:10.1016/s0169-555x(02)00160-5

Major, J. J., and Pierson, T. C. (1992). Debris Flow Rheology: Experimental Analysis of fine-grained Slurries. *Water Resour. Res.* 28, 841–857. doi:10.1029/91WR02834

Manville, V., Hodgson, K. A., and White, J. D. L. (1998). Rheological Properties of a Remobilised-tephra Lahar Associated with the 1995 Eruptions of Ruapehu Volcano, New Zealand. *New Zealand J. Geology. Geophys.* 41, 157–164. doi:10.1080/00288306.1998.9514800

Manville, V., Major, J., and Fagents, S. (2013). "Modeling Lahar Behavior and Hazards," in *Modeling Volcanic Processes: The Physics and Mathematics of Volcanism*. Editors S. Fagents, T. Gregg, and R. Lopes (Cambridge University Press), 300–330. doi:10.1017/CBO9781139021562.014

Mariño, J., Rivera, M., Cacya, L., Thouret, J.-C., Macedo, O., Salas, G., et al. (2007). *Mapa de los peligros volcánicos del Misti. Ingemmet, Proyecto Multinacional Andino, IRD*. Lima: LMV, Instituto de Geofísica UNAM, UNSA, Universidad Católica de Santa Maria, INDECI, Gobierno regional de Arequipa, Municipalidad provincial de Arequipa, PREDES, SENAMHI.

Martelli, K. M. (2011). *The Physical Vulnerability of Urban Areas Facing the Threat of Inundation from Lahars and Floods: Application to the City of Arequipa, Peru. (Unpublished) PhD Thesis*. Clermont-Ferrand: Laboratoire Magmas et Volcans, Université Blaise Pascal, 345.

Mead, S. R., Magill, C., Lemiale, V., Thouret, J.-C., and Prakash, M. (2017). Examining the Impact of Lahars on Buildings Using Numerical Modelling. *Nat. Hazards Earth Syst. Sci.* 17, 703–719. doi:10.5194/nhess-17-703-2017

Municipalidad Provincial de Arequipa (2011). Plan de contingencia ante precipitaciones pluviales en la Provincia de Arequipa 2010–2011. Available at: http://www.muniarequipa.gob.pe/descargas/emergencia/plan.pdf.

Nagata, M. (1999). *Una introducción a las inundaciones en el área urbana de Arequipa. Informe sobre las Torrenteras en Arequipa*. Lima: INDECI-IGP-ORSTOM, 99.

National Weather Service (2022). NOAA. Available at: https://www.weather.gov.phi/FlashFloodingDefinition (Accessed on March 18, 2022).

Nigro, E., and Faella, C. (2008). "Effects of Debris Flow on Buildings," in *Urban Habitat under Catastrophic Events. Proceedings COST Action 26, Final Conference*. Editor F. M. Mazzolani (CRC Press), 420–429.

O'Brien, J., Julien, P., and Fullerton, W. (1993). Two-dimensional Water Flood and Mudflow Simulation. *J. Hydraul. Eng.* 119 (2), 244–261. doi:10.1061/(ASCE)0733-9429(1993)119:2(244)

O'Brien, J. S., and Julien, P. Y. (1988). Laboratory Analysis of Mudflow Properties. *J. Hydraul. Eng.* 114 (8), 877–887. doi:10.1061/(ASCE)0733-9429(1988)114:8(877)

Oehler, J.-F., Thouret, J.-C., Solikhin, A., and Ettinger, S. (2014). *High Resolution DEMs Based on HSR PLEIADES Images: Applications to the Merapi Volcano (Indonesia) and the City of Arequipa Close to the Misti Volcano (Peru)*. Yogjakarta, Indonesia: COV8 meeting 9-13 September. Abstract and poster.

Pallares, C., Fabre, D., Thouret, J.-C., Bacconnet, C., Charca-Chura, J. A., Martelli, K., et al. (2015). Geological and Geotechnical Characteristics of Recent Lahar Deposits from El Misti Volcano in the City Area of Arequipa, South Peru. *Geotech Geol. Eng.* 33, 641–660. doi:10.1007/s10706-015-9848-x

Paquereau-Lebti, P., Fornari, M., Roperch, P., Thouret, J.-C., and Macedo, O. (2008). Paleomagnetism, Magnetic Fabric, and 40Ar/39Ar Dating of Pliocene and Quaternary Ignimbrites in the Arequipa Area, Southern Peru. *Bull. Volcanol.* 70, 977–997. doi:10.1007/s00445-007-0181-y

Paquereau-Lebti, P., Thouret, J.-C., Wörner, G., Fornari, M., and Macedo, O. (2006). Neogene and Quaternary Ignimbrites in the Area of Arequipa, Southern Peru: Stratigraphical and Petrological Correlations. *J. Volcanology Geothermal Res.* 154, 251–275. doi:10.1016/j.jvolgeores.2006.02.014

Phillips, C. J., and Davies, T. R. H. (1991). Determining Rheological Parameters of Debris Flow Material. *Geomorphology* 4, 101–110. doi:10.1016/0169-555X(91)90022-3

Pierson, T. C., and Costa, J. E. (1987). A Rheologic Classification of Subaerial Sediment-Water Flows. *Rev. Eng. Geol.* VII, 1–12. doi:10.1130/reg7-p1

Pierson, T. C. (1980). Debris Flows: An Important Process in High Country Gully Erosion. *J. Tussok Grassland Mountain Lands Inst. (N.Z.)* 39, 3–14. doi:10.1002/ESP.3760050302

Pierson, T. C. (2005). "Hyperconcentrated Flow – Transitional Process between Water Flow and Debris Flow," in *Debris Flow Hazards and Related Phenomena*. Editors M. Jakob and O. Hunger (Springer), 159–202.

Pitman, E. B., and Le, L. (2005). A Two-Fluid Model for Avalanche and Debris Flows. *Phil. Trans. R. Soc. A.* 363 (1832), 1573–1601. doi:10.1098/rsta.2005.1596

Prieto, J. A., Journeay, M., Acevedo, A. B., Arbelaez, J. D., and Ulmi, M. (2018). Development of Structural Debris Flow Fragility Curves (Debris Flow Buildings Resistance) Using Momentum Flux Rate as a hazard Parameter. *Eng. Geology.* 239, 144–157. doi:10.1016/j.enggeo.2018.03.014

Regional de Arequipa, G. (2014). *Plan regional de gestión del riesgo de desastre 2014-2021*. Arequipa, 90.

Rickenmann, D. (1999). Empirical Relationships for Debris Flows. *Nat. Haz.* 19, 47–77. doi:10.1023/a:1008064220727

Rickenmann, D. (1991). Hyperconcentrated Flow and Sediment Transport at Steep Slopes. *J. Hydraulic Eng.* 117, 1419–1439. doi:10.1061/(asce)0733-9429(1991)117:11(1419)

Sandri, L., Thouret, J.-C., Constantinescu, R., Biass, S., and Tonini, R. (2014). Long-term Multi-hazard Assessment for El Misti Volcano (Peru). *Bull. Volcanol.* 76, 771–797. doi:10.1007/s00445-013-0771-9

Savage, S. B., and Hutter, K. (1989). The Motion of a Finite Mass of Granular Material Down a Rough Incline. *J. Fluid Mech.* 199, 177–215. doi:10.1017/s0022112089000340

Schilling, S. P. (2014). Laharz_py: GIS Tools for Automated Mapping of Lahar Inundation hazard Zones. *U.S. Open File Rep. 2014-* 1073, 78. doi:10.3133/ofr20141073

Scott, K. M. (1988). *Origins, Behavior, and Sedimentology of Lahars and Lahar-Runout Flows in the Toutle-Cowlitz River System*. Washington, DC: U.S. Geol. Surv. Prof. Paper 1447-A, 74.

Scott, K. M., Vallance, J. W., Kerle, N., Luis Macías, J., Strauch, W., and Devoli, G. (2005). Catastrophic Precipitation-Triggered Lahar at Casita Volcano, Nicaragua: Occurrence, Bulking and Transformation. *Earth Surf. Process. Landforms* 30 (1), 59–79. doi:10.1002/esp.1127

SENAMHI (2013). *Periodo de lluvias 2013 en la región Arequipa y su relación con el Cambio Climático. Foro Regional Desastre, Reconstrucción y desarrollo en escenario de cambio climático*. Lima: Arequipa – emergencia.

Silgado, E. (1978). *Historia de los sismos más notables ocurridos en el Perú 1513-1974*. Lima: Instituto de Geología y Minería.

Stoffel, M., Khodri, M., Corona, C., Guillet, S., Poulain, V., Bekki, S., et al. (2015). Estimates of Volcanic-Induced Cooling in the Northern Hemisphere over the Past 1,500 Years. *Nat. Geosci* 8, 784–788. doi:10.1038/ngeo2526

Takahashi, T. (2014). *Debris Flow, Mechanics, Prediction and Countermeasures*. 2nd ed. Balkema: CRC Press Taylor and Francis Group, 448.

Tavera, H. (2020). *Análisis y evaluación de los patrones de sismicidad y escenarios sísmicos en el borde Occidental del Perú*. Lima: Instituto Geofísico del Perú, 66.

Thouret, J.-C., Antoine, S., Magill, C., and Mead, S. (2020). Lahars and Debris Flows: Characteristics and Impacts. *Earth-sci Rev.* 201. doi:10.1016/j.earscirev.2019.103003

Thouret, J.-C., Enjolras, G., Martelli, K., Santoni, O., Luque, J. A., Nagata, M., et al. (2013). Combining Criteria for Delineating Lahar- and Flash-Flood-Prone hazard and Risk Zones for the City of Arequipa, Peru. *Nat. Hazards Earth Syst. Sci.* 13, 339–360. doi:10.5194/nhess-13-339-2013

Thouret, J.-C., Ettinger, S., Guitton, M., Santoni, O., Magill, C., Martelli, K., et al. (2014). Assessing Physical Vulnerability in Large Cities Exposed to Flash Floods and Debris Flows: the Case of Arequipa (Peru). *Nat. Hazards* 73 (3), 1771–1815. doi:10.1007/s11069-014-1172-x

Thouret, J.-C., Finizola, A., Fornari, M., Legeley-Padovani, A., Suni, J., and Frechen, M. (2001). Geology of El Misti Volcano Near the City of Arequipa, Peru. *Geol. Soc. Amer Bull.* 113 (12), 1593–1610. doi:10.1130/0016-7606(2001)113<1593:goemvn>2.0.co;2

Thouret, J.-C., Legros, F., Gourgaud, A., Salas, G., Juvigné, E., Gilot, E., et al. (1995). Un exemple de prévision des risques volcaniques au Pérou méridional (région d'Arequipa), fondé sur l'étude de l'activité éruptive récente du strato-volcan El Misti. *C.-R. Acad. Sci. Paris Série IIa, Géomatériaux Tome* 320, 923–929.

Thouret, J.-C., Santoni, O., Arapa, E., Belizario, J., Guerrero, A., Rodriguez, D., et al. (2018). *Methodology for Assessing Exposure, Physical Vulnerability and Risk Due to Mass Flows in the City of Arequipa, Peru*, 9. Washington DC: AGU Fall meeting–14. *December, Abstract ID* 366543*, Poster* NH41D-1143. Session NH41D: The Collection of Natural Hazard, Exposure, and Vulnerability Data for Use in Risk Assessments and Other Novel Purposes.

Thouret, J.-C., Suni, J., Eissen, J.-Ph., and Navarro, P. (1999). Assessment of Volcanic Hazards in the Arequipa Area Based on the Eruptive History of Misti Volcano, Southern Peru. *Zeit. Geomor.* 114, 89–112. doi:10.0044/2798/99/0114-0089

Thouret, J. C. (2018). "Hazard and Risk Mapping," in *The Arequipa- El Misti Case and Other Threatened Cities* (Presses Universitaires Blaise Pascal, MSH Clermont-FerrandTerritoires H.S), 1154. (in Spanish, English, French), Clermont-Ferrand.

UN-DESA (2018). *The World's Cities in 2018: Data Booklet*. New York: UN Population Division, UN DESA, 29.

Vallance, J. W., and Iverson, R. M. (2015). "Lahars and Their Deposits," in *The Encyclopedia of Volcanoes*. 2nd ed. (Elsevier & Academic Press), 649–664. doi:10.1016/b978-0-12-385938-9.00037-7

Vallance, J. W. (2000). "Lahars," in *The Encyclopedia of Volcanoes*. 1st ed. (San Diego: Academic Press), 601–616.

Vargas-Franco, R., Thouret, J.-C., Delaite, G., van Westen, C., Sheridan, M. F., Siebe, C., et al. (2010). "Mapping and Assessing Volcanic Hazards and Risk in the City of Arequipa, Peru, Based on GIS Techniques," in *Stratigraphy and Geology of Volcanic Areas*. Editors G. Groppelli and L. Viereck-Goette (Geol. Soc. Am. Spec Publ SPE464), 265–280.

Williams, R., Stinton, A. J., and Sheridan, M. F. (2008). Evaluation of the Titan2D Two-phase Flow Model Using an Actual Event: Case Study of the 2005 Vazcún Valley Lahar. *J. Volcanol. Geoth. Res.* 177, 760–766. doi:10.1016/j.jvolgeores.2008.01.045

Woolhiser, D. (1975). "Simulation of Unsteady Overland Flow," in. *Unsteady flow in open channels*. Editors K. Mahmood and V. Yevjevich (Water Resources Publication), Vol. 2, 485–508.

Xue, N. (2016). *Analyse de l'endommagement post-écoulement par un traitement statistique de données extraites d'images satellite et de chroniques- L'exemple de la ville d'Arequipa, Pérou. Ms. Sci. (Unpubl.) Report, Laboratoire Magmas et Volcans*. Clermont-Ferrand: Universite Blaise Pascal, 52.

Zanchetta, G., Sulpizio, R., Pareschi, M. T., Leoni, F. M., and Santacroce, R. (2004). Characteristics of May 5-6, 1998 Volcaniclastic Debris Flows in the Sarno Area

(Campania, Southern Italy): Relationships to Structural Damage and hazard Zonation. *J. Volcanology Geothermal Res.* 133, 377–393. doi:10.1016/s0377-0273(03)00409-8

Zeng, C., Cui, P., Su, Z., Lei, Y., and Chen, R. (2015). Failure Modes of Reinforced concrete Columns of Buildings under Debris Flow Impact. *Landslides* 12, 561–571. doi:10.1007/s10346-014-0490-0

Conflict of Interest: The authors declare that the research was conducted in the absence of any commercial or financial relationships that could be construed as a potential conflict of interest.

Publisher's Note: All claims expressed in this article are solely those of the authors and do not necessarily represent those of their affiliated organizations or those of the publisher, the editors, and the reviewers. Any product that may be evaluated in this article, or claim that may be made by its manufacturer, is not guaranteed or endorsed by the publisher.

Copyright © 2022 Thouret, Arapa, Charbonnier, Guerrero, Kelfoun, Cordoba, Rodriguez and Santoni. This is an open-access article distributed under the terms of the Creative Commons Attribution License (CC BY). The use, distribution or reproduction in other forums is permitted, provided the original author(s) and the copyright owner(s) are credited and that the original publication in this journal is cited, in accordance with accepted academic practice. No use, distribution or reproduction is permitted which does not comply with these terms.